

A Physical Model for $z \sim 2$ Dust-Obscured Galaxies*

Desika Narayanan^{1†‡}, Arjun Dey², Christopher C. Hayward¹, Thomas J. Cox^{1,3§},
 R. Shane Bussmann⁴, Mark Brodwin^{1¶}, Patrik Jonsson⁵, Philip F. Hopkins^{6||},
 Brent Groves⁷, Joshua D. Younger^{1,8**}, and Lars Hernquist¹

¹Harvard-Smithsonian Center for Astrophysics, 60 Garden St., Cambridge, Ma 02138

²National Optical Astronomy Observatory, 950 N. Cherry Avenue, Tucson, Arizona, 85719

³Observatories of the Carnegie Institute of Washington, 813 Santa Barbara St., Pasadena, Ca, 91101

⁴Steward Observatory, University of Arizona, 933 N Cherry Avenue, Tucson, Arizona, 85721

⁵Santa Cruz Institute for Particle Physics, University of California, Santa Cruz, Santa Cruz, Ca

⁶Department of Astronomy and Theoretical Astrophysics Center, University of California Berkeley, 601 Campbell Hall, Berkeley, Ca 94720

⁷Sterrewacht Leiden, Leiden University, Neils Bohrweg 2, Leiden 233-CA, The Netherlands

⁸Institute for Advanced Study, Einstein Drive, Princeton, NJ, 08544

Submitted to MNRAS

ABSTRACT

We present a physical model for the origin of $z \sim 2$ Dust-Obscured Galaxies (DOGs), a class of high-redshift ULIRGs selected at $24 \mu\text{m}$ which are particularly optically faint ($F_{24\mu\text{m}}/F_R > 1000$). By combining N -body/SPH simulations of high redshift galaxy evolution with 3D polychromatic dust radiative transfer models, we find that luminous DOGs (with $F_{24} \gtrsim 0.3 \text{ mJy}$ at $z \sim 2$) are well-modeled as extreme gas-rich mergers in massive ($\sim 5 \times 10^{12} - 10^{13} M_\odot$) halos, with elevated star formation rates ($\sim 500 - 1000 M_\odot \text{yr}^{-1}$) and/or significant AGN growth ($\dot{M}_{\text{BH}} \gtrsim 0.5 M_\odot \text{yr}^{-1}$), whereas less luminous DOGs are more diverse in nature. At final coalescence, merger-driven DOGs transition from being starburst dominated to AGN dominated, evolving from a “bump” to a power-law shaped mid-IR (IRAC) spectral energy distribution (SED). After the DOG phase, the galaxy settles back to exhibiting a “bump” SED with bluer colors and lower star formation rates. While canonically power-law galaxies are associated with being AGN-dominated, we find that the power-law mid-IR SED can owe both to direct AGN contribution, as well as to a heavily dust obscured stellar bump at times that the galaxy is starburst dominated. Thus power-law galaxies can be either starburst or AGN dominated. Less luminous DOGs can be well-represented either by mergers, or by massive ($M_{\text{baryon}} \approx 5 \times 10^{11} M_\odot$) secularly evolving gas-rich disc galaxies (with $\text{SFR} \gtrsim 50 M_\odot \text{yr}^{-1}$). By utilising similar models as those employed in the SMG formation study of Narayanan et al. (2010), we investigate the connection between DOGs and SMGs. We find that the most heavily star-forming merger driven DOGs can be selected as Submillimetre Galaxies (SMGs), while both merger-driven and secularly evolving DOGs typically satisfy the BzK selection criteria. The model SEDs from the simulated galaxies match observed data reasonably well, though Mrk 231 and Arp 220 templates provide worse matches. Our models provide testable predictions of the physical masses, dust temperatures, CO line widths and location on the $M_{\text{BH}}-M_{\text{bulge}}$ relation of DOGs. Finally, we provide public SED templates derived from these simulations.

Key words: cosmology:theory–galaxies:formation–galaxies:high-redshift–galaxies:starburst–galaxies:ISM–galaxies:ISM–ISM:dust

* This paper is dedicated to the original DOG himself, Cordozar Calvin Broadus, Jr.

† E-mail: dnarayanan@cfa.harvard.edu

‡ CfA Fellow

§ Carnegie Fellow

¶ W.M. Keck Postdoctoral Fellow

|| Miller Fellow

** Hubble Fellow

1 INTRODUCTION

Redshift $z \sim 2$ is a rich epoch for understanding galaxy formation and evolution. During this time period, the bulk of the cosmic stellar mass was assembled (Dickinson et al. 2003; Rudnick et al. 2006), and the star formation rate and quasar space densities are both near their peaks (Bouwens et al. 2004; Hopkins 2004; Hopkins et al. 2007; Shaver et al. 1996).

In the local Universe, infrared (IR) selection of galaxies is an efficient means of selecting galaxies undergoing significant star formation (e.g., Arp 220), and possibly hosting optically-obscured active galactic nuclei (AGN; e.g., Mrk 231, NGC 6240). By analogy, at higher redshifts, IR selection techniques select galaxies which are major contributors to the cosmic star formation rate density, far-IR background, and progenitors of the present-day massive galaxy population. Indeed, ultraluminous infrared galaxies (ULIRGs; $L_{\text{IR}} > 10^{12} L_{\odot}$) at $z \sim 2$ appear to contribute substantially to the infrared luminosity density (Pérez-González et al. 2005; Caputi et al. 2007; Reddy et al. 2008; Hopkins et al. 2010; Hopkins & Hernquist 2010), and the $z > 0.7$ star formation rate density (Le Flocc'h et al. 2005; Shi et al. 2009).

A well-studied sample of galaxies selected for their FIR properties at $z \sim 2$ are Submillimetre Galaxies (SMGs), chosen in blank field surveys for their redshifted cool dust emission at 850 μm above $F_{850} \gtrsim 5$ mJy. These galaxies are in a transient starburst phase (e.g., Swinbank et al. 2004; Menéndez-Delmestre et al. 2007; Younger et al. 2008a; Michałowski et al. 2009), host rapidly growing supermassive black holes (e.g., Alexander et al. 2005, 2008), and reside in extremely massive $\sim 5 \times 10^{12} M_{\odot}$ halos (Blain et al. 2004). While these galaxies represent an important sub-population of infrared-luminous galaxies at the epoch of peak galaxy formation, there is some concern that a selection at 850 μm may be missing significant populations of high-redshift ULIRGs with warmer dust temperatures (e.g., Bussmann et al. 2009; Chapman & Casey 2009; Casey et al. 2009; Huang et al. 2009; Younger et al. 2009). As such, alternative selection techniques for identifying $z \sim 2$ ULIRGs have become desirable.

With the launch of the *Spitzer Space Telescope*, surveys at 24 μm have uncovered a population of ULIRGs at $z \sim 2$ (e.g., Rigby et al. 2004; Donley et al. 2007; Yan et al. 2007; Farrah et al. 2008; Soifer et al. 2008; Lonsdale et al. 2009; Huang et al. 2009, and references therein). Recently, Dey et al. (2008, hereafter, D08; see also Fiore et al. (2008)) presented an efficient means of identifying high-redshift ULIRGs which are both mid-infrared luminous and optically faint. Specifically, by imposing a nominal selection criteria of $R-[24] > 14$ (roughly corresponding to a flux density ratio $F_{24}/F_{\text{R}} > 1000$; formally $F_{24}/F_{\text{R}} > 960$) and $F_{24} > 0.3$ mJy, D08 found a sample of ULIRGs with a relatively narrow redshift distribution (centered at $\langle z \rangle = 1.99$ with $\sigma_z = 0.5$) which exhibit heavy reddening of the intrinsic UV flux and strong rest-frame 8 μm emission (Houck et al. 2005; Fiore et al. 2008). D08 refer to these galaxies as Dust-Obscured Galaxies (DOGs)¹.

DOGs exhibit a range of luminosities, though AGN-dominated galaxies tend to preferentially dominate the bright end of the 24 μm flux density distribution (Brand et al. 2006; Weedman et al. 2006a,b; Dey et al. 2008; Fiore et al. 2008, 2009; Sacchi et al. 2009). The DOGs with the highest 24 μm flux den-

sities ($F_{24} > 0.8$ mJy) have bolometric infrared luminosities (L_{IR}) $\sim 10^{13} L_{\odot}$ (Bussmann et al. 2009; Tyler et al. 2009). As a population, the subset of $F_{24} > 0.3$ mJy galaxies which are also DOGs contribute around a quarter of the total infrared luminosity density at $z \sim 2$ (Dey et al. 2008), and constitute $\sim 60\%$ of the total contribution by $z \sim 2$ ULIRGs. It is clear that DOGs are a cosmologically significant population of galaxies with diverse observational characteristics.

Broadly, 24 μm -selected ULIRGs at $z \sim 2$ (including DOGs) appear to fall into two categories based on their mid-IR IRAC SEDs: those with a power-law shape and those which exhibit a bump at observed $\lambda \sim 5$ μm corresponding to the 1.6 μm rest frame stellar photospheric bump (hereafter, these are referred to as PL galaxies and bump galaxies, respectively). Bump galaxies are thought to be dominated by star formation, with the bump (at rest-frame 1.6 μm) originating from starlight. PL galaxies are thought to have their mid-IR SED dominated by AGN continuum emission (Weedman et al. 2006b; Donley et al. 2007; Yan et al. 2007; Murphy et al. 2009). In support of this scenario, PL galaxies have SEDs which are reasonably represented by that of a Mrk 231 template (Bussmann et al. 2009; Tyler et al. 2009), and tend to show relatively compact optical morphologies ($R_e \sim 1 - 6$ kpc; Melbourne et al. 2008, 2009; Bussmann et al. 2009). On the other hand, bump galaxies are typically polycyclic aromatic hydrocarbon (PAH)-rich, show PAH equivalent widths consistent with being star formation dominated (Yan et al. 2005; Sajina et al. 2007; Farrah et al. 2008; Desai et al. 2009; Huang et al. 2009), and are more often morphologically resolved into multiple components (Bussmann et al. 2009). However, Fiore et al. (2008, 2009) have argued that even these less luminous galaxies may harbor heavily obscured AGN.

DOGs are massive galaxies, with stellar masses $M_{\star} > 10^{10-11} M_{\odot}$ (Bussmann et al. 2009; Lonsdale et al. 2009; Huang et al. 2009), and cluster in group-sized halos of order ($M_{\text{DM}} \approx 10^{12-13} M_{\odot}$; Brodwin et al. 2008). The clustering is luminosity-dependent, with more luminous DOGs inhabiting more massive halos. Since the more luminous DOGs also tend to exhibit power-law SEDs, it follows that PL DOGs cluster more strongly than the lower luminosity bump DOGs.

Although much progress has been made in understanding DOGs in a relatively short time period, a myriad of fundamental questions regarding their physical nature exist. Are DOGs preferentially isolated galaxies or mergers (or both)? Does the 24/R criterion select galaxies at a particular evolutionary point? How are bump DOGs and PL DOGs related - are they distinct galaxy populations, or possibly related via an evolutionary sequence? How are DOGs related to other coeval high-redshift populations (e.g., the SMGs, *BzK* galaxies, etc.)?

Numerical simulations can offer complementary information to the observations in hand, and provide insight into the aforementioned questions. In particular, by coupling radiative transfer modeling with hydrodynamic simulations of galaxy evolution, one can precisely mimic local and high-redshift observational selection functions, and directly relate observed trends to physical conditions in the model galaxies (e.g., Jonsson 2006; Jonsson et al. 2006, 2010; Lotz et al. 2008; Narayanan et al. 2010; Younger et al. 2009).

Previously, we have utilised similar methods to investigate the formation and evolution of high-redshift Submillimetre Galaxies Narayanan et al. (2009, 2010, C. Hayward et al. in prep.). Here, we build upon these efforts by utilising similar models as those employed in Narayanan et al. (2009) and Narayanan et al. (2010).

¹ We note that while this paper nominally focuses on 24 μm -selected galaxies which additionally have $24/R > 1000$, the results of this paper are generally applicable to the 24 μm -bright ($F_{24} > 0.3$ mJy) $z \sim 2$ ULIRG population.

This will allow us not only to investigate a potential formation mechanism for DOGs, but to explore the potential connection between $z \sim 2$ ULIRGs selected for their 24 μm brightness, and those selected in the submillimetre.

The paper is organised as follows. In § 2, we detail our numerical methods. In § 3, we describe the formation of $z \sim 2$ DOGs, and explain the evolution of the 24/R ratio and the relationship between bump and PL DOGs. In § 4, we discuss the physical requirements necessary to form a DOG, and whether mergers are necessary; In § 5, we detail the relationship between DOGs, SMGs and *BzK* galaxies. In § 6, we relate our model to existing observations, and make testable predictions. In § 7, we provide discussion. We conclude in § 8.

Throughout this paper, we utilise a fiducial DOG selection criteria $24/R > 1000$ and $F_{24} > 300 \mu\text{Jy}$, consistent with the DOGs sample in D08. We note again that while we focus on these 24 μm selected galaxies which are optically faint (DOGs), the results are generally applicable to most 24 μm -selected $z \sim 2$ ULIRGs. Throughout, we assume a cosmology with $\Omega_\Lambda = 0.7$, $\Omega_m = 0.3$ and $h = 0.7$. Finally, we note that the models presented here are not cosmological in nature. As such, all non-evolutionary plots should be taken to represent ranges of expected values and colors, rather than true expected distributions.

2 NUMERICAL METHODS

Our methodology is as follows. We first run a suite of Smoothed-particle hydrodynamics (SPH) simulations of binary gas-rich galaxy mergers over a range of baryonic masses and merger mass ratios. The mergers are between idealised disc galaxies. We additionally run three isolated disc galaxy simulations as a control. These simulations represent potential physical models for $z \sim 2$ 24 μm sources. We then investigate the UV-mm wave SEDs of these galaxies utilising a 3D dust radiative transfer code in post-processing. In what follows, we describe the details of these numerical simulations, and outline both the input parameters, as well as the assumptions made.

2.1 Hydrodynamics

The hydrodynamic evolution of the galaxies was simulated utilising a modified version of the publicly available N -body/SPH code, GADGET-2 (Springel 2005). GADGET-2 follows the dynamical evolution of the dark matter, ISM, stars and black holes in the simulated galaxies, and explicitly conserves both energy and entropy (Springel & Hernquist 2002).

The ISM is considered to comprise of a two-phase medium via a sub-grid model (Springel & Hernquist 2003). In this model, cold clouds are assumed to be embedded in a hotter, pressure-confining phase. The cold phase may convert to the hotter phase via evaporation from supernovae heating, and similarly the hot phase may cool into cold gas. This ISM is pressurised by heating from supernovae. Numerically, this is handled via an effective equation of state (hereafter EOS; see Figure 4 of Springel et al. 2005b). Here, we assume the stiffest equation of state which stabilises the disc against run-away fragmentation. We explore the consequences of relaxing this assumption in § 2.2.2.

The star formation rate in the simulations is dependent on the density of cold gas (defined here as gas which has reached the floor of the cooling curve, $T = 10^4 \text{K}$) as $\text{SFR} \propto \rho_{\text{gas}}^{1.5}$. The normalisation of this relation is set such that the simulated star formation rate

surface density scales with the gas surface density in agreement with local observations (Kennicutt 1998; Cox et al. 2006).

Black holes are included in the simulations as collisionless particles. These particles stochastically accrete matter according to a Bondi-Hoyle-Lyttleton parameterisation when a particle comes within a smoothing length of the black hole sink particle. To model the impact of thermal feedback from accreting black holes, a fraction of the accreted mass energy (here, 0.5%) is reinjected thermally and spherically into the surrounding ISM (Springel et al. 2005b). The fraction of accreted mass energy which couples back to the ISM is set by matching the normalisation to the local $M_{\text{BH}} - \sigma$ relation (though note that the slope is a natural consequence of the AGN feedback; Di Matteo et al. 2005).

The progenitor disc galaxies are initialised with a Hernquist (1990) dark matter halo profile. The choice of concentration and virial radius for a halo of a given mass was motivated by cosmological N -body simulations, then scaled to match the expected redshift evolution (Bullock et al. 2001; Robertson et al. 2006). The halo for our fiducial model (DOG10, Table 1) has a $z=0$ concentration $c = 11.0$ and spin parameter $\lambda = 0.033$. We initialise our discs to reside at $z=3$, so that our simulated mergers occur around $z \sim 2$. We consider initial virial velocities in the range 225-500 km s^{-1} , resulting in dark matter halo masses of $\sim 10^{12} M_\odot$ - $10^{13} M_\odot$, consistent with the DOG clustering measurements by Brodwin et al. (2008). The halos are populated with exponential discs whose disc scale lengths follow the Mo et al. (1998) prescriptions.

The discs for model galaxies are initialised with gas fractions $f_g \equiv \text{gas}/(\text{gas} + \text{stars}) = 0.8$. Simulation tests by Narayanan et al. (2010) have shown that high-redshift mergers initialised with this gas fraction result in $f_g \approx 0.2 - 0.4$ at the time when the galaxy may be viewed as an SMG, which is comparable to observations (e.g. Bouché et al. 2007; Tacconi et al. 2008; Daddi et al. 2009; Tacconi et al. 2010). While gas fractions in DOGs are observationally unconstrained, based on an observed overlap between the luminous DOG and SMG populations (e.g., Pope et al. 2008; Brodwin et al. 2008), we consider this assumption reasonable. In order to investigate any potential dependence on gas fraction, we have run a subset of our simulations with initial gas fractions $f_g = 0.4, 0.6$ as well. The results from all initialisations are qualitatively similar, and we include both in our plots to increase the simulation sample size. The gravitational softening lengths are set at $100 \text{h}^{-1} \text{pc}$ for baryons and $200 \text{h}^{-1} \text{pc}$ for dark matter. Because structure in the ISM clearly exists below these scale lengths, we employ a subgrid specification to the ISM for the radiative transfer calculations. This will be discussed in the following two subsections.

In this paper, we consider 16 simulations, with initial conditions listed in Table 1. The simulations (and nomenclature) here are nearly identical² to those in Narayanan et al. (2009) and Narayanan et al. (2010)'s studies of SMG formation. This will facilitate direct comparisons between the DOG population and high-redshift SMGs. When we refer to investigating a fiducial merger, this will refer to model DOG10 with initial $f_g = 0.8$.

² The primary difference between the simulations run here and those employed in Narayanan et al. (2009) is in the assumptions of the evolving dust mass (see the next section). Here, we tie the dust mass to the metallicity, whereas in Narayanan et al. (2009), the dust mass is tied to the gas mass. This makes little difference during the merger event, though can have some effects on the optical flux during the inspiral phase.

Table 1. DOGs are ordered with decreasing halo mass (and grouped by mergers and isolated galaxies, such that the isolated galaxies have the prefix 'i' in their name). Column 1 is the name of the model used in this work. We emphasise that these models are nearly identical to those employed in the SMG formation study by Narayanan et al. (2010) and Narayanan et al. (2009). This will facilitate the comparison of these models with SMGs (§ 5.1). Columns 2 and 3 give the virial velocity and halo mass of the galaxies. Column 4 is the total baryonic mass of the system. Column 5 is the merger mass ratio. Columns 6 & 7 are initial orientations for disc 1, Columns 8 & 9 are for disc 2. The orientation angles are with respect to the merger plane (such that $\theta, \phi = 0$ would be a coplanar merger). Column 10 lists the initial gas fraction of the simulation.

Model	V_c (km s^{-1})	M_{DM} M_\odot	M_{bar} M_\odot	Mass Ratio	θ_1	ϕ_1	θ_2	ϕ_2	f_g
DOG1	500:500	$1.25 \times 10^{13}; 1.25 \times 10^{13}$	1.1×10^{12}	1:1	30	60	-30	45	0.8,0.6,0.4
DOG2	500:500	$1.25 \times 10^{13}; 1.25 \times 10^{13}$	1.1×10^{12}	1:1	360	60	150	0	0.8
DOG3	500:500	$1.25 \times 10^{13}; 1.25 \times 10^{13}$	1.1×10^{12}	1:1	-109	-30	71	-30	0.8
DOG4	500:320	$1.25 \times 10^{13}; 3.4 \times 10^{12}$	6.9×10^{11}	1:3	30	60	-30	45	0.8,0.6,0.4
DOG5	500:320	$1.25 \times 10^{13}; 3.4 \times 10^{12}$	6.9×10^{11}	1:3	360	60	150	0	0.8
DOG6	500:320	$1.25 \times 10^{13}; 3.4 \times 10^{12}$	6.9×10^{11}	1:3	-109	-30	71	-30	0.8
DOG7	500:225	$1.25 \times 10^{13}; 1.2 \times 10^{12}$	6.0×10^{11}	1:10	30	60	-30	45	0.8,0.6,0.4
DOG8	500:225	$1.25 \times 10^{13}; 1.2 \times 10^{12}$	6.0×10^{11}	1:10	360	60	150	0	0.8
DOG9	500:225	$1.25 \times 10^{13}; 1.2 \times 10^{12}$	6.0×10^{11}	1:10	-109	-30	71	-30	0.8
DOG10	320:320	$3.4 \times 10^{12}; 3.4 \times 10^{12}$	2.9×10^{11}	1:1	30	60	-30	45	0.8,0.6,0.4
DOG11	320:320	$3.4 \times 10^{12}; 3.4 \times 10^{12}$	2.9×10^{11}	1:1	360	60	150	0	0.8
DOG12	320:320	$3.4 \times 10^{12}; 3.4 \times 10^{12}$	2.9×10^{11}	1:1	-109	-30	71	-30	0.8
DOG13	225:225	$1.2 \times 10^{12}; 1.2 \times 10^{12}$	1.0×10^{11}	1:1	30	60	-30	45	0.8,0.6,0.4
iDOG1	500	1.25×10^{13}	5.5×10^{11}	—	N/A	N/A	N/A	N/A	0.8,0.6,0.4
iDOG2	320	3.4×10^{12}	1.5×10^{11}	—	N/A	N/A	N/A	N/A	0.8,0.6,0.4
iDOG3	225	1.2×10^{12}	5×10^{10}	—	N/A	N/A	N/A	N/A	0.8,0.6,0.4

2.2 Radiative Transfer

2.2.1 General Methods

We extract synthetic SEDs from our SPH simulations in post-processing utilising the 3D polychromatic Monte Carlo radiative transfer code, SUNRISE (Jonsson 2006; Jonsson et al. 2010). SUNRISE considers the propagation of UV through mm-wave photons through a dusty medium, and operates on an adaptive mesh. Here, we summarise the aspects of the code most relevant to this study, and refer the reader to Jonsson et al. (2010) for the most current detailed description of the underlying algorithm.

Dust radiative transfer may be thought of in terms of sources and sinks. Here, the sources of radiation are stellar clusters, AGN and dust grains. The stellar clusters emit a spectrum calculated by STARBURST99 (Leitherer et al. 1999; Vázquez & Leitherer 2005), where the ages and metallicities of the stars are known from the SPH simulations. The stellar particles present in the simulation's initial conditions are assumed to have formed over a constant star formation history for ~ 250 Myr (where this time was chosen by dividing the stellar mass of the first simulation snapshot by the SFR at that time). That said, the rest-frame UV and mid-IR (which dominates the wavelength regime of interest for DOGs) is contributed mainly by young (< 100 Myr) stars (and their surrounding HII regions), and thus our results are largely insensitive to the choice of star formation history. We assume a Kroupa IMF for these calculations, suggested by observations of $z \sim 2$ SMGs (Tacconi et al. 2008).

The AGN input spectrum utilises the luminosity-dependent templates of Hopkins et al. (2007) of type I quasars. The template spectrum includes torus hot dust emission, and is based on the mid-IR SED template of Richards et al. (2006). The normalisation of the input spectrum is set by the total bolometric luminosity of the

black hole(s), which is determined by their mass accretion rate: $L_{\text{AGN}} = \eta \dot{M}_{\text{BH}} c^2$. Here, η is assumed to be 10%. The AGN are included in all simulations investigated here (mergers as well as secularly evolving galaxies).

The sinks of radiation are dust grains in the ISM. The emission from stars and AGN undergo scattering, absorption and remission as they propagate through the ISM. Because the ISM substructure is not resolved by our hydrodynamic simulations, we employ subgrid modeling techniques which we explore in the following subsection. Eight model cameras are set up isotropically around the galaxy to observe the merger. The emergent flux is determined by the number of photons that escape the galaxy in a given camera's direction.

SUNRISE calculates the dust temperature of the grains self-consistently, and assumes that the dust and radiation field are in radiative equilibrium utilising the methodology of Juvela (2005) for calculating the converged radiation field. In this methodology, when photons are absorbed in a grid cell, the dust temperature is updated. A new photon packet is then emitted from this cell which has an SED equal to the difference between the SED associated with the updated dust temperature, and that from the old one. This procedure is iterated upon until the radiation field has converged (Jonsson et al. 2010). Consequently, both the AGN and the starburst are involved in determining the dust temperature across all the grid cells.

PAHs are emitted by the HII regions, PDRs, and the diffuse dust in the galaxy. Carbonaceous dust grains with sizes $a < 100 \text{ \AA}$ are assumed to have characteristics of PAH molecules. A fraction of these PAH molecules (following Jonsson et al. 2010, we take this value to be 50%) emit a template spectrum, and the remaining fraction emit thermally. The PAH template is a linear combination of Lorentzian profiles, and the fraction of PAHs emitting the template is chosen to fit *Spitzer* IRS observations of local galaxies

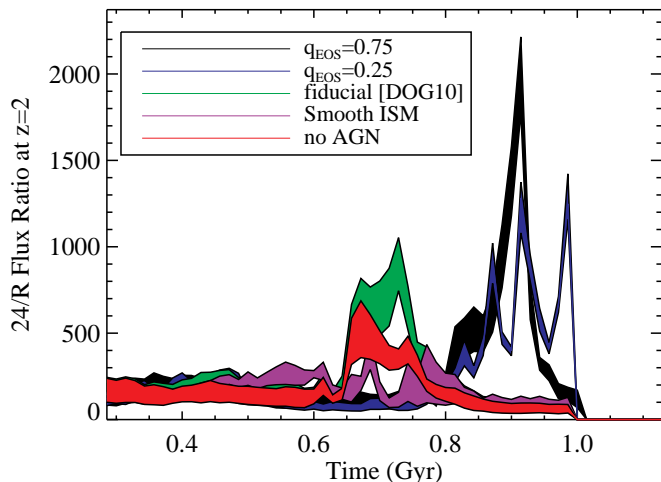


Figure 1. Evolution of $24/R$ ratio for our fiducial model (DOG10) while varying the ISM specification and inclusion of AGN. See text in § 2.2.2 for details.

(Dopita et al. 2005; Groves et al. 2008; Jonsson et al. 2010). Their absorption is calculated utilising the Li & Draine (2001) cross sections. Varying this fraction changes the PAH luminosity (which can affect the $24 \mu\text{m}$ flux density at $z=2$). We have performed test simulations exploring the range of PAH fractions, from 0 to 1. Generally, the trends presented in this paper are insensitive to the inclusion of PAHs, though the normalisation of some trends can be. That is to say, the magnitude of the $24/R$ ratio is dependent on the fraction of emitting PAHs, though the evolutionary trends in the $24/R$ ratio are not. Tests investigating the limits (e.g. either 0% or 100% of carbonaceous grains with sizes $a < 100\text{\AA}$ emit as PAHs) show that the observed $24 \mu\text{m}$ flux density of our model galaxies varies at most by a factor of ~ 2 (when observed at $z=2.0$). We note that PAHs are not explicitly destroyed by the AGN.

The evolving dust mass is calculated assuming a constant dust to metals ratio of 0.4, consistent with models and observations of both local Universe galaxies, as well as those at higher redshifts (Dwek 1998; Vladilo 1998; Calura et al. 2008). The distribution and mass of interstellar dust is determined by the galaxy evolution simulations. We use the Weingartner & Draine (2001) dust grain model with $R \equiv A_V/E_{B-V} = 3.15$, as updated by Draine & Li (2007). This model includes silicates and graphites. We note that silicate absorption features are not put in by hand into this model - rather their occurrence is the result of modeled radiative transfer effects.

All photometric quantities in this paper are convolved with the appropriate instrument filter sensitivity function. Throughout this paper, all flux densities and flux density ratios come from both galaxies in the simulation box. While the simulation box is 100 kpc on a side, the nuclei of the galaxies (where the bulk of the emission arises from) never stray more than ~ 50 kpc from each other. This is roughly comparable to the *Spitzer* $24 \mu\text{m}$ beam at $z=2$. Hence, during all the relevant stages of the interaction, both galaxies would appear as a single (blended) source in *Spitzer* $24 \mu\text{m}$ surveys.

2.2.2 ISM Specification and Other Free Parameters

The ISM in our simulations is unresolved below the hydrodynamic resolution limit of ~ 100 pc. In order to model obscuration below these scales, we employ subgrid methods. In the remainder of this subsection, we discuss the effects of the subgrid assumptions on our final results. For the reader unfamiliar with the main results of this paper, it may be worthwhile returning to this section after reading through the main results to better understand the implications of our subgrid techniques. In this section, we will refer to Figure 1 frequently, which summarises our comparison of varying ISM treatments. In this figure, we vary assumptions regarding the ISM and AGN for our fiducial merger, DOG10 (with 80% initial gas fraction), and plot the evolution of the $24/R$ ratio. The thickness of each lightcurve owes to sightline variations in the SED.

The young stellar clusters (with ages < 10 Myr) are assumed to reside in their nascent birthclouds, and have their spectrum reddened accordingly. The birthclouds are comprised of HII regions and photodissociation regions (PDRs), whose sizes and temperatures are calculated with the 1 dimensional photoionisation code MAPPINGSIII (Groves et al. 2008). The HII regions evolve as one-dimensional mass-loss bubbles (Castor et al. 1975) and absorb much of the ionising UV radiation from the stellar clusters. In fact, the HII regions dominate the $24 \mu\text{m}$ continuum (observed-frame at $z=2$) flux density during starbursts.

The time-averaged covering fraction of PDRs is a free parameter, and can be related to the PDR clearing time scale as $f_{\text{PDR}} = \exp(-t/t_{\text{clear}})$. Here, we take the PDR covering fraction to be unity ($f_{\text{PDR}} = 1$) which essentially means that massive O and B stars are assumed to be surrounded by their nascent birthclouds for the entirety of their lives (as the PDR clearing timescale is then longer than the lives of these stars; see Figure 6 of Groves et al. 2008). While f_{PDR} is an unconstrained parameter, some evidence exists that in local mergers a molecular interstellar medium with a large volume filling factor may blanket nuclear O and B stars for the majority of their lives (Downes & Solomon 1998; Sakamoto et al. 1999). This suggests that a large PDR covering fraction may be a reasonable assumption in massive starbursts. The assumption of $f_{\text{PDR}} = 1$ is conservative: removing the cold birthclouds typically increases the $24 \mu\text{m}$ flux density (observed at $z=2.0$) (as emission from the HII regions can escape more unhindered).

One potential issue is that the MAPPINGSIII SEDs are parameterised in terms of their compactness, which is dependent both on the stellar cluster masses and the ISM pressure (see e.g. equations 9-13 of Groves et al. 2008). The pressures seen in the central regions of the most massive high- z mergers exceed the largest ones available in the MAPPINGSIII lookup tables by a factor of ~ 10 -100. This means that in reality the MAPPINGSIII HII/PDR SED will be hotter than those at the saturated values used here (see, Figure 5 of Groves et al. 2008). Because the stellar/HII/PDR SEDs dominate primarily during the peak starburst phase of a merger, the net effect of this is that we are likely *underestimating* the duty cycle of the DOG phase during merger-driven starbursts in our simulated galaxy sample. Because our inclusion of the MAPPINGSIII SEDs errs on the side of more conservative models, we proceed with this caveat in mind.

Our simulations have no information about the structure of the ISM below the resolution limit outside of a stellar cluster's birthcloud. Effectively, what this means is that the radiative transfer models here do not account for absorption by GMCs outside of a given stellar cluster's birthcloud (Jonsson et al. 2010). To place an upper limit on the potential attenuation from the cold ISM, we

have run test cases where we assume that each grid cell is uniformly filled with dust and gas with the mass returned from the SPH simulations. This effectively assumes that all dust that would be associated with GMCs in the ISM has a volume filling fraction of unity. Because the mass in the birthclouds is 'borrowed' from this gas mass budget, in this special scenario we require that $f_{\text{PDR}} = 0$ in order to avoid potential double-counting issues. In this extreme case, the ISM is optically thick at mid-infrared (rest-frame) wavelengths, and the SED has a larger proportion of its flux at longer wavelengths. The purple curve in Figure 1 shows the evolution of the relatively depressed $24/R$ ratio for this "Smooth ISM" case. We note that while the $24/R$ ratio in this Smooth ISM model is not as large as the other cases, the galaxy's SED is still quite red. In this case, a larger fraction of the power in the SED is shifted into the FIR; as such, this galaxy would likely be selectable by e.g. *Herschel* surveys.

Our choice of equation of state may have an effect on the star formation history and structure of the ISM in the model galaxies as well. Nominally, we utilise the full Springel & Hernquist (2003) multi-phase EOS which simulates the pressurisation of the ISM owing to supernovae heating. This is somewhat stiffer than an isothermal EOS (the stiffest EOS is shown by the solid curve in Figure 4 of Springel et al. 2005b, the isothermal EOS is the dashed line). Referring to this figure, the effective EOS employed can be quantified by a 'softening parameter' such that $q_{\text{EOS}} = 1$ represents the stiffest EOS which aims to account for SNe pressurisation of the ISM. Similarly, $q_{\text{EOS}} = 0$ represents an isothermal EOS.

Because we use the stiff EOS ($q_{\text{EOS}} = 1$), the gas is relatively pressurised which retards fragmentation. This affects both the star formation history as well as the structure of the ISM (galaxies with a softer EOS will be more clumpy which may affect optical depths). To investigate the consequences of our choice of EOS, we have examined the evolution of a fiducial galaxy merger, DOG10 with softer EOSs ($q_{\text{EOS}} = 0.25$ and $q_{\text{EOS}} = 0.75$, linear interpolations between isothermal and $q_{\text{EOS}} = 1$).

In Figure 1, we show the $24/R$ lightcurves for our fiducial model, with the aforementioned modifications to soften the EOS (black and blue curves). The general effect of the softening of the EOS is to cause the ISM to become more unstable to fragmentation, and reduce optical depths toward the central regions. Because of this, the observed SED is hotter for the $q_{\text{EOS}} = 0.75$ and 0.25 cases than the fiducial DOG10, and the peak $24 \mu\text{m}$ flux density a factor of a few higher. Softening the equation of state increases the likelihood that a given simulation will be selectable as a DOG.

There is some evidence that discs at high redshift may indeed be clumpy. Both observations (e.g. Elmegreen et al. 2007; Daddi et al. 2008; Genzel et al. 2006; Elmegreen et al. 2009; Förster Schreiber et al. 2009) and models (e.g. Bournaud et al. 2008; Dekel et al. 2009; Elmegreen 2009; Ceverino et al. 2010; Elmegreen & Burkert 2010) suggest that disc galaxies at high- z contain relatively large clumps of gas. However, despite this, we choose to utilise the simulations with the stiffest equation of state ($q_{\text{EOS}} = 1$). The reasons follow. First, with respect to simulating the formation of DOGs, this is the middle-of-the-road choice amongst our ISM assumptions. For example, examination of Figure 1 shows that while a softer EOS more easily produces DOGs, a smooth ISM suppresses them. The model with birthclouds (and no other cold GMCs) and a stiff EOS has a test lightcurve which falls in between the two extremes. Second, we can constrain the models somewhat by the gas fractions at the time of merger. If we assume that mergers represent a reasonable model for the formation of high-redshift Submillimetre Galaxies (e.g. Tacconi et al. 2006,

2008; Narayanan et al. 2009, 2010, though see Davé et al. 2009 for counter-arguments), then the gas fractions in the model galaxies at the time of merger/peak submm flux density should be comparable to those inferred from observations. Indeed, Narayanan et al. (2010) showed that the gas fractions at peak coalescence were indeed $\sim 40\%$, comparable to the measurements of Bouché et al. (2007) and Tacconi et al. (2008). However, because our simulations do not include the infall of primordial gas from the IGM, there is no way to replenish the gas once it is consumed by star formation. Thus, by utilising a softer EOS and increasing the level of disc fragmentation/star formation, the models quickly run out of gas and render the galaxy relatively gas poor during the peak submm phase. Tests show that the simulation with $q_{\text{EOS}} = 0.75(0.25)$ have gas fractions of $\sim 20(10)\%$ during their final coalescence/peak-submm phases. In this sense, our usage of a stiff EOS is a requirement to match certain physical properties of the most extreme high- z ULIRGs, necessitated by limitations of the models. Moreover, in the interest of making a more direct comparison with our previous attempts at modeling high- z ULIRGs (to wit, the SMG population Narayanan et al. 2009, 2010), we utilise the stiffest EOS and birthcloud model to remain consistent with the initial conditions chosen for those models.

To summarise our exploration of the effects of ISM substructure on the radiative transfer, we expect clumpiness of the ISM to exist on three scales: on the scale of birthclouds around young stellar clusters; in other GMCs outside of the birthclouds; and on $\sim\text{kpc}$ scales as seen in observed discs at high- z (e.g. Elmegreen et al. 2007, 2009). Our inclusion of the MAPPINGSIII calculations accounts for some obscuration on the birthcloud scale, and our parameter search with the EOS has tested the possible effects of larger clumps on the radiative transfer. With respect to obscuration by GMCs outside of the parent birthcloud, the current generation of simulations only allow us to test the limiting cases of a smooth obscuring ISM with a volume filling fraction of unity. The results of these tests on the models are summarised in Figure 1.

Finally, we can explore the role AGN play in our model for DOG formation. AGN heat the surrounding dust and contribute to rest frame $8\mu\text{m}$ thermal emission. This both increases the observed $24/R$ ratio, as well as the duty cycle over which the galaxy has extremely red colors. The effect of not including AGN can be seen in the red curve in Figure 1.

3 FORMATION AND EVOLUTION OF DOGS

3.1 Physical Evolution of a Merger

The formation of ULIRGs through mergers has a long history (e.g., Sanders et al. 1988; Sanders & Mirabel 1996). We therefore begin our investigation of DOGs with the ansatz that DOGs originate in gas rich galaxy mergers at high redshift. We will then go on to explore under what circumstances DOGs may be represented by non-merging galaxies (§ 4), and show that as observations probe sufficiently lower $24 \mu\text{m}$ flux density limits, less extreme conditions are sufficient to form DOGs.

We first briefly orient the reader as to the generic physical evolution of a high-redshift binary gas rich galaxy merger. Here, we focus on fiducial model DOG10 (Table 1). DOG10 is a 1:1 $M_{\text{DM}} \approx 6 \times 10^{12} M_{\odot}$ merger. Figure 2 shows the evolution of the morphology of DOG10 as viewed from a single SUNRISE camera. The boxes are 100 kpc/h on a side, and the galaxy is observed at $z=2$ (with the observed $24 \mu\text{m}$, R and B -band emission mapped

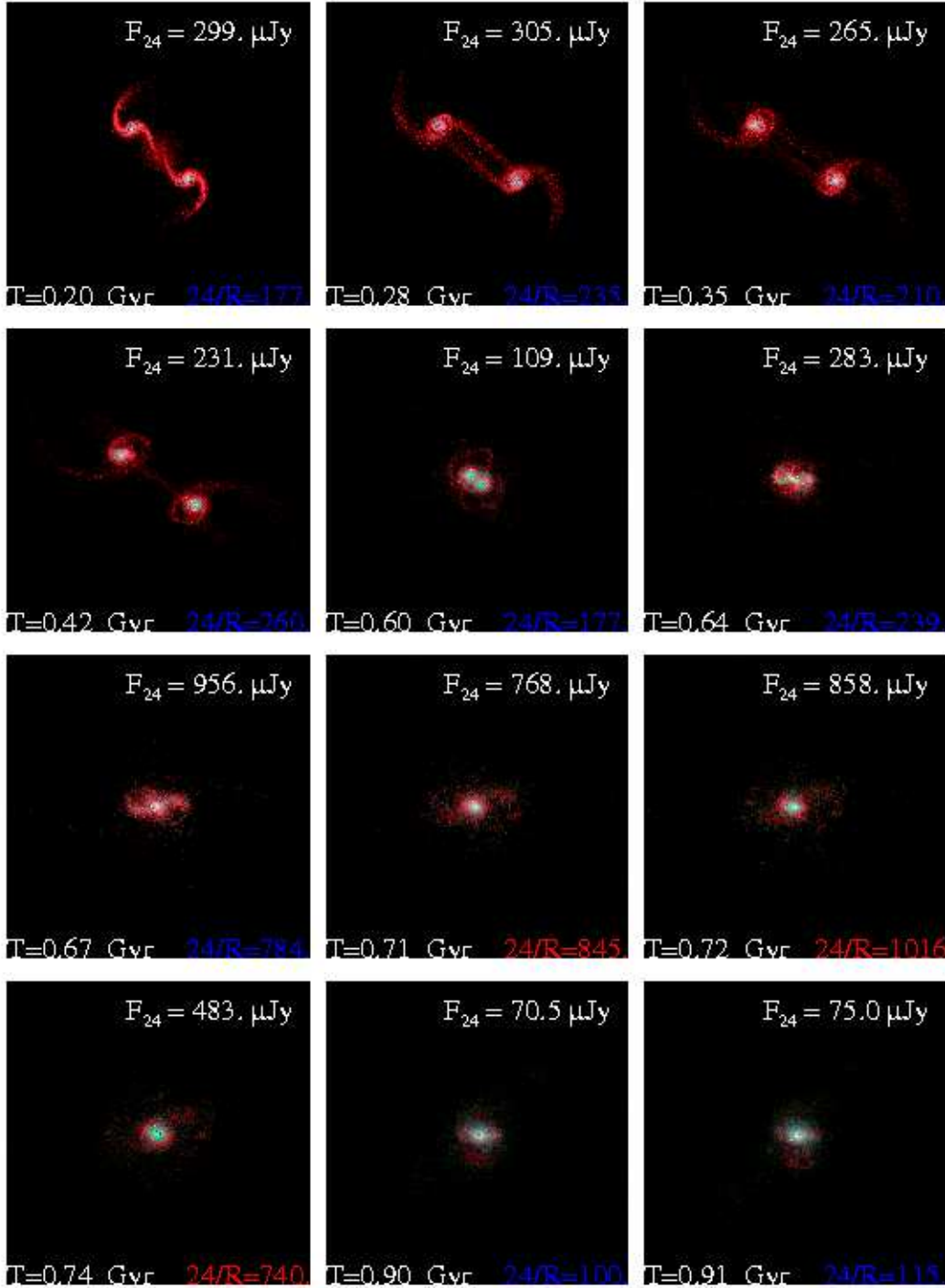


Figure 2. Morphology of fiducial merger, DOG10, modeled at redshift $z=2$. Colors are (observed-frame) MIPS 24 μm , R -band, and B -band mapped onto red, green and blue. Each panel is 100 kpc/h on a side, and the time stamp, 24 μm flux density, and $24/R$ ratio is denoted in each panel. The color of the $24/R$ label represents if the mid-IR SED exhibits a bump or power-law nature (to be discussed in § 3.3), where blue labels show bump galaxies, and red labels PL galaxies. Mergers naturally form DOGs. As the merger progresses, the galaxy becomes redder owing to increased 24 μm flux density powered by the dust-enshrouded starburst. Upon final coalescence, when the SFR peaks, the galaxy is red enough that it may be observed as a DOG ($24/R > 1000$). Subsequent contribution from a growing AGN will allow the galaxy to transition from a bump DOG to a PL DOG.

onto red, green and blue). DOG10 is a very similar model to as the fiducial SMG (SMG10) studied in Narayanan et al. (2009). We will present a more detailed comparison between DOGs and SMGs in § 5.1.

In Figure 3, we show the evolution of the SFR, black hole accretion rate, and bolometric luminosity of DOG10. The first passage of the galaxies induces a $\sim 200 M_{\odot} \text{yr}^{-1}$ starburst. This elevated star formation rate is largely sustained for $\sim 5 \times 10^8 \text{yr}$ while the galaxies inspiral toward final coalescence. As such, by the time of coalescence, the galaxy system builds up a $\sim 10^{11} M_{\odot}$ bulge (Narayanan et al. 2010).

When the galaxies approach for final coalescence, tidal torquing on the gas funnels large quantities into the nucleus of the merged system (Barnes & Hernquist 1991, 1996; Mihos & Hernquist 1994, 1996; Springel et al. 2005b), inducing a massive $\sim 1000 M_{\odot} \text{yr}^{-1}$ starburst. Concomitantly, inflows fuel central black hole accretion. In the mergers modeled here, the black hole accretion rate can approach $\sim 1-2 M_{\odot} \text{yr}^{-1}$. The associated AGN feedback contributes (along with gas consumption by star formation) to terminating the starburst, and may render the black hole optically luminous for a short period of time as feedback and gas depletion clear sightlines (Springel et al. 2005b; Hopkins et al. 2005a,b), accounting for the observed population of bright quasars (Hopkins et al. 2006, 2008). The contribution of newly formed stars and an embedded AGN drive the $\sim 10^{13} L_{\odot}$ bolometric luminosity during the merger. It is during the final merger, when the starburst, black hole accretion rate and bolometric luminosity are all near their peak ($T \approx 0.65-0.75 \text{ Gyr}$; i.e., the shaded region in Figure 3) that we expect the infrared luminosity of the model galaxy to peak (Jonsson et al. 2006; Younger et al. 2009; Narayanan et al. 2010).

3.2 The Evolution of the $24/R$ Ratio in Mergers

In Figure 4, we plot the evolution of the $24/R$ ratio for fiducial merger DOG10 placed at $z=2$. As a reminder, Figures 2 and 3 serve as a reference for the morphology, black hole accretion rate, SFR, and bolometric luminosity for this galaxy. The grey shaded region shows the range of $24/R$ ratios as seen from 8 isotropically placed cameras outside the model galaxy, and thus reflects the dependence of the $24/R$ ratio on viewing angle. The yellow shaded region shows when the galaxy could be detected above the nominal $F_{24} > 300 \mu\text{Jy}$ detection threshold at $z=2$. We plot the $850 \mu\text{m}$ lightcurve as well (with units on the right ordinate), though defer discussion of this aspect of the figure until § 5.1). We additionally note when the galaxy would be a bump galaxy, and when it would be a PL galaxy (as the red/blue colors in the $24/R$ lightcurve), but defer discussion of this aspect of the galaxy's evolution to § 3.3.

Massive mergers at high redshift naturally produce DOGs during their final coalescence. The galaxy appears the reddest during the starburst/AGN activity associated with final coalescence (in our fiducial DOG, we note that it is formally above the $24/R > 960$ threshold for only a brief period of time. More massive models [e.g. DOG1] form DOGs for longer duty cycles. DOG10 is, to some degree, the rough minimum galaxy mass necessary in our simulations to form a DOG). The observed $24 \mu\text{m}$ thermal emission comes from two sources. During the inspiral phase, warm dust in the diffuse ISM dominates the $24 \mu\text{m}$ emission. At times of elevated SFR (e.g., during final coalescence; $T \approx 0.65 \text{ Gyr}$), HII regions additionally contribute a substantial fraction of the observed $24 \mu\text{m}$ thermal emission allowing the galaxy to be selected in $24 \mu\text{m}$ surveys. As gas consumption and the wind from the AGN terminate

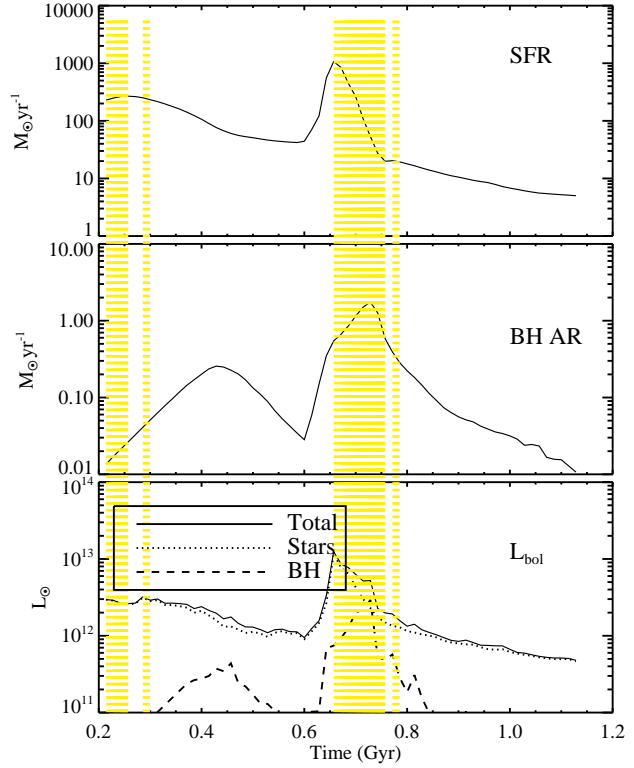


Figure 3. Evolution of star formation rate, black hole accretion rate, and bolometric luminosity for fiducial merger model DOG10. The bolometric luminosity includes contributions from both stars and black holes. The yellow shaded region shows when the galaxy would be selected in a $F_{24} > 300 \mu\text{Jy}$ flux limited survey (the gap in the yellow region denotes a short time this particular simulated merger falls slightly below the $F_{24} > 300 \mu\text{Jy}$ flux density limit). The SFR, black hole accretion and luminosity all peak near when the galaxy is undergoing final coalescence. It is during this time that the galaxy system is expected to peak in infrared luminosity. We note that the black hole accretion rate and SFR are averages over 10 Myr intervals.

both the starburst (Springel et al. 2005a) and black hole growth (Younger et al. 2008b), the $24/R$ ratio fades. Soon thereafter, the $24 \mu\text{m}$ flux density drops (with the bolometric luminosity of the galaxy) such that the galaxy would no longer be detectable with current instruments.

The $24/R > 1000$ DOG criterion selects star-forming galaxies which have large quantities of obscuring dust in the diffuse ISM. The copious rest-frame UV photons produced by the starburst are reprocessed into rest-frame $8 \mu\text{m}$ thermal radiation by dust both within the HII regions and in the diffuse ISM. Though this point may seem trivial, it is to be underscored that $z \approx 2$ star-forming galaxies without large columns of dust in the diffuse ISM may still be selected as $24 \mu\text{m}$ -bright galaxies (owing to the reprocessing of some of their UV photons in HII regions), but will not be reddened enough in their observed $24/R$ to be selected as DOGs. We demonstrate this explicitly in Figure 5, where we show the $24 \mu\text{m}$ and R -band lightcurves for our fiducial model (DOG10) both including diffuse dust (the fiducial model) and neglecting it. For the model neglecting diffuse dust, we still include HII regions surrounding stellar clusters. It is clear that the HII regions are responsible for a substantial fraction of the observed $24 \mu\text{m}$ flux density. However,

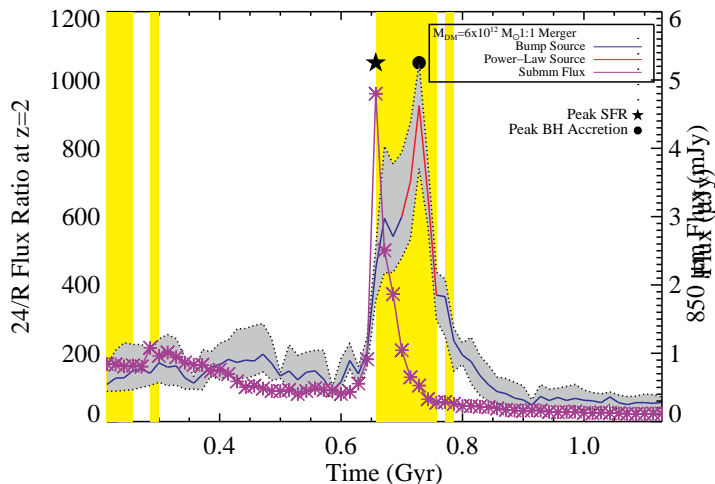


Figure 4. $24/R$ and $850 \mu\text{m}$ light curves for fiducial model DOG10, modeled at $z=2$. The blue/red line is the sightline-averaged $24/R$ ratio as a function of time, and the color in this line denotes when the galaxy may be visible as a bump galaxy (blue) or PL galaxy (red). (See § 3.3 for a discussion regarding the transition from bump to PL mid-IR SED.) The grey shaded region highlights the range of $24/R$ ratios seen over 8 isotropic viewing angles, and thus reflects the sightline dependence of the $24/R$ ratio. The yellow shaded region shows when the galaxy’s $24 \mu\text{m}$ flux density is above a fiducial limit of $300 \mu\text{Jy}$. The break in the yellow shaded region is a short phase when the galaxy drops just below $300 \mu\text{Jy}$. The black filled star and circle near the top show when the star formation rate and black hole accretion rates peak, respectively. The $850 \mu\text{m}$ flux density is overlaid as the purple curve, and has its units on the right axis. As the galaxy passes through its starburst dominated phase, it may be visible as both a Submillimetre Galaxy (with $F_{850} > 5 \text{ mJy}$), as well as a bump galaxy. The galaxy eventually transitions to becoming a PL galaxy, and may be either starburst or AGN dominated during this time.

the diffuse dust is important in absorbing the UV radiation which escapes the HII regions; without this attenuation, the excess radiation which escapes the galaxy causes the normalisation of the $24/R$ ratio to fall significantly below the DOG selection criteria.

3.3 Evolution of Bump DOG to Power-law DOG

As discussed in § 1 (see also D08), the mid-IR spectra of DOGs come in two flavors: those characterised by a ‘bump’ at $\sim 5 \mu\text{m}$, and those exhibiting a power-law rise in the SED (Dey et al. 2008). Bump features in the mid-IR SED of $z \sim 2$ galaxies are thought to originate from a combination of thermal emission from lower mass stars at rest-frame $1.6 \mu\text{m}$, and emission from massive stars which show a local minimum in their atmospheric opacity at this wavelength (John 1988; Simpson & Eisenhardt 1999; Farrah et al. 2008). Similarly, the PL shape in the mid-IR spectra of $z \sim 2$ galaxies is canonically associated with the dominant presence of AGN continuum (though, as we will show, the PL SED can originate in starburst dominated galaxies).

In a merger-driven model for DOG formation, there is a natural evolution in the mid-IR SEDs of $z \sim 2$ DOGs from bump-like to PL-like as the merger progresses. For the purposes of our analysis, we fix our model galaxies at $z=2$, and define a bump galaxy

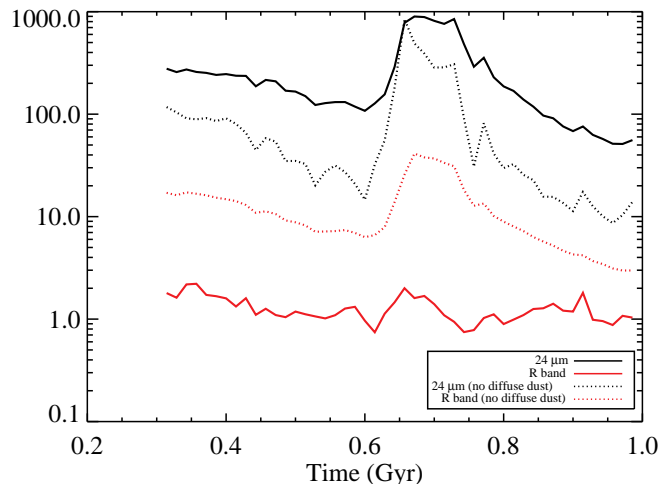


Figure 5. $24 \mu\text{m}$ and R -band lightcurves for the fiducial model (DOG10) both including diffuse dust (solid lines) and neglecting it (dotted lines). We remind the reader that all models in this paper include diffuse dust with the exception of the dotted lightcurves in this figure. The models without diffuse dust still include HII regions surrounding stellar clusters. It is clear that the HII regions are responsible for a large fraction of the $24 \mu\text{m}$ flux. The diffuse dust is important in absorbing the UV radiation which escapes the HII regions; without this attenuation, the excess radiation which escapes the galaxy causes it to appear optically bright, and thus not selectable as a DOG.

utilising a simple peak-finding method³ such that $S_3 < S_5$ and $S_5 > S_8$ (where S_3 , S_5 , and S_8 correspond to the filter-convolved fluxes from IRAC channels 1,2 and 4, respectively). Similarly, we define a PL galaxy as one where $S_3 < S_5 < S_8$. Returning to Figure 4, we now see that when we utilise this criteria for classifying the bump and PL phase of the galaxy’s evolution, there is a transition during the merger from a bump galaxy to a PL galaxy (where the bump phase is denoted by the blue segment of the line, and the PL phase by the red one). Comparing with the morphology (Figure 2), it is evident that this transition occurs during final coalescence.

We can understand the details of the origin of the bump to PL transition more explicitly by examining the evolution of the SEDs of DOGs during the final coalescence stage. In Figure 6, we present the sightline-averaged SED from fiducial galaxy DOG10 as it evolves through its final coalescence phase. The observed SED is shown by the black solid line in each panel. The blue dashed SED represents the input STARBURST99 SED⁴, and the red dotted curve the input AGN template SED. Both the stellar and AGN SEDs are unreddened by diffuse dust in the galaxy (though the stars are reddened by HII regions and PDRs). We list the time stamp of each panel for comparison with the morphology (Figure 2), and global $24/R$ light curve (Figure 4), and quote the $24/R$ ratio in each panel. The $24/R$ ratio is color coded based on if the DOG is a bump galaxy (blue), or PL galaxy (red).

³ We note that this definition of ‘bump’ versus ‘powerlaw’ mid-IR SEDs is similar to that used by Farrah et al. (2008), and is simpler to implement than the power-law fitting method used by D08.

⁴ More specifically, the blue dashed line is the STARBURST99 input SED after it has passed through the HII regions and PDRs surrounding stellar cluster utilising MAPPINGSIII.

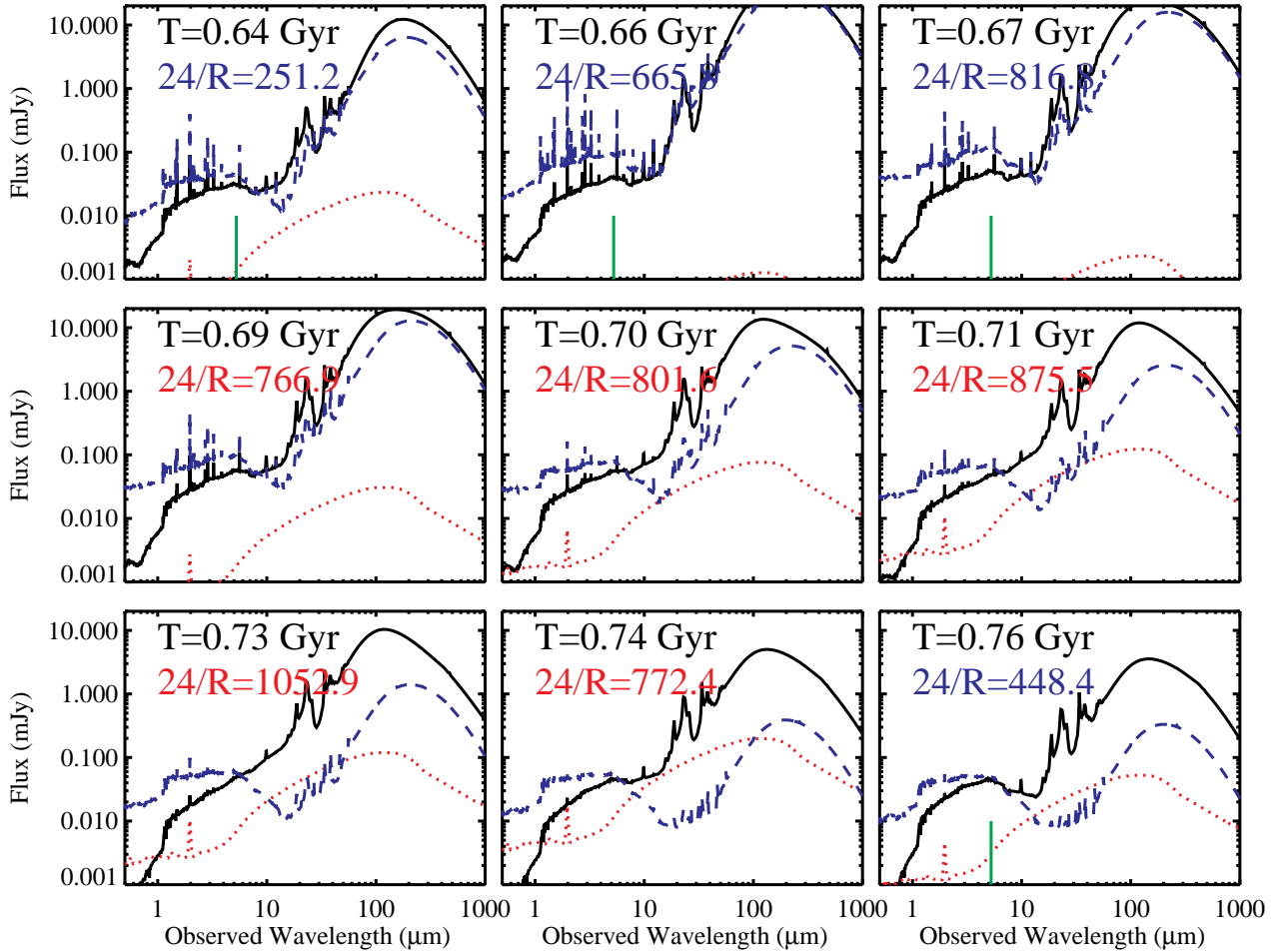


Figure 6. Model SEDs for 9 snapshots of fiducial galaxy DOG10 as it evolves through its final coalescence DOG phase. The black line is the sightline-averaged observed SED (at $z=2$). The blue dashed line represents the stellar SED (after passing through HII regions and PDRs), and the red dotted line is the unattenuated AGN spectrum. The SEDs are all redshifted to $z=2$, and the abscissa is the observed-frame wavelength. The $24/R$ ratio is listed along with the time for each snapshot, and the color of the $24/R$ ratio represents when the galaxy would be selected as a bump galaxy (blue) versus a PL galaxy (red). A green vertical line is placed at the rough location of the redshifted stellar bump in the snapshots which are bump galaxy. We note that we label the galaxy as a bump or PL galaxy regardless of whether it classifies as a DOG by the fiducial $24/R$ criteria. The galaxy’s DOG phase begins as a bump DOG (e.g., $T = 0.67$ Gyr). As the merger progresses, the galaxy will be selected as a PL DOG, either owing to dust attenuation of the stellar bump (even at times when the AGN contribution is not particularly strong; e.g., $T = 0.70$ Gyr), or to direct contribution from the AGN continuum (e.g., $T = 0.74$ Gyr). It is important to note that even some sources that may appear as bump galaxies by eye (e.g. $T = 0.69$ Gyr) may not be classified as such when convolving with IRAC filters. Finally, we note that while only a single snapshot in this Figure is formally a DOG, the duty cycle increases with increasing galaxy mass. The fiducial DOG represents a rough lower limit to the galaxy mass which forms DOGs.

In the early stages of the DOG phase (near the beginning of final coalescence, e.g., $T = 0.67$ Gyr), the mid-IR SED shows the characteristic stellar bump associated with a star-formation dominated infrared luminosity. As the merger evolves, the mid-IR SED becomes best characterised by a power-law shape. PL galaxies can arise from either starburst-dominated or AGN-dominated DOGs. Starburst-dominated PL galaxies owe their origin to large columns of dust obscuration associated with the final merging. To see this, consider panel $T = 0.70$ Gyr in Figure 6. During the merger, the intrinsic stellar flux density at $\lambda \lesssim 5 \mu\text{m}$ can be extinguished by up to an order of magnitude. This can force the SED to look power-law-like, even while the AGN contribution at these wave-

lengths is small. The galaxy then evolves into an AGN-dominated PL galaxy. Here, the AGN SED contributes substantially to the observed SED at $\lambda \gtrsim 8 \mu\text{m}$, again giving a power-law mid-IR shape (e.g., $T = 0.74$ Gyr). As is clear, then, PL mid-IR SEDs from $z \sim 2$ galaxies may represent either starburst dominated or AGN dominated galaxies. The relationship between the AGN contribution to PL mid-IR SEDs in $z \sim 2$ $24 \mu\text{m}$ sources will be explored in more detail in a forthcoming paper (D. Narayanan et al., in prep.).

Finally, we note that in the post-merger stage, the galaxy exhibits bluer colors with a bump-like SED. These ULIRGs are reminiscent of those detected which are less extreme than DOGs

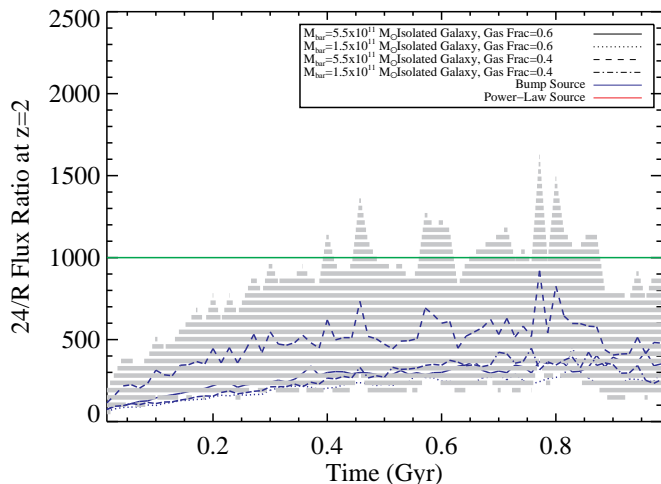


Figure 7. Evolution of sightline averaged $24/R$ lightcurves for the most massive two of the model isolated galaxies in Table 1 (iDOG1 and iDOG2) are shown as blue lines. Both gas fractions are plotted for iDOG1 and iDOG2. The range of colors owing to viewing angle of the reddest galaxy is shown by the grey-hatched region. While isolated galaxies typically are not red enough to satisfy the DOG criteria, the most massive, metal-rich ones certainly can when in edge-on viewing angles.

in deep *Spitzer* surveys Yan et al. (2005, 2007); Lonsdale et al. (2009); Yan et al. (2010).

4 THE PHYSICAL FORM OF DOGS: ARE MERGERS NECESSARY?

Thus far, we have seen that gas rich galaxy mergers at high redshift provide a plausible means for forming luminous DOGs. Furthermore, this mechanism for DOG formation suggests a picture for connecting bump DOGs and PL DOGs. This leads to a natural question: are mergers a necessary prerequisite for the formation of DOGs?

We begin with Figure 7, where we show the evolution of the $24/R$ ratio for the most massive isolated galaxies in Table 1. We plot the lightcurves for both gas initial fractions modeled - 40% and 60%. The lightcurves are sightline averaged, and we show the sightline-averaged dispersion for the reddest galaxy through the grey-shaded region. Generally, isolated galaxies are not quite red enough to satisfy the fiducial $24/R > 1000$ criteria for DOG selection. This said, the most massive, dust-rich ones can represent DOGs. For example, the 40% gas fraction, $M_{\text{bar}} \approx 5 \times 10^{11} M_{\odot}$ model (which starts with nearly solar metallicity in the closed-box model) approaches DOG-like redness. That said, the most massive, dust-rich isolated galaxies can be selected as DOGs when in an edge-on configuration.

We can further investigate the relative role isolated discs and mergers play toward $z \sim 2$ ULIRG formation in Figure 8, where we plot the SFR versus the $24 \mu\text{m}$ flux density (and rest-frame $8 \mu\text{m}$ luminosity) at $z=2$ for every snapshot in our simulation sample that has a $24/R$ ratio > 1000 . We discriminate both between mergers and isolated galaxies, as well as whether the galaxy is a bump or PL DOG. The larger symbols are galaxies which would also be detectable as SMGs, though we defer discussion of this aspect until § 5.1. Mergers populate the bulk of the luminous ($F_{24} >$

$300 \mu\text{Jy}$) DOG population in this diagram. These systems, which are extremely gas/dust rich, become red enough to be selected as DOGs during close passages and final coalescence (e.g., Figure 4). Mergers provide an efficient means for generating the starburst and/or AGN activity to heat the dust sufficiently that the galaxy is visible at $24 \mu\text{m}$ above $300 \mu\text{Jy}$. Nominally, we find a minimum $\text{SFR} \gtrsim 500 M_{\odot} \text{yr}^{-1}$ necessary when AGN activity is negligible to power $F_{24} > 300 \mu\text{Jy}$ sources. Similarly, for DOGs powered by AGN, we find minimum AGN accretion rates of $\dot{M}_{\text{BH}} \gtrsim 0.5 M_{\odot} \text{yr}^{-1}$ are required to power the brightest DOGs.

At lower $24 \mu\text{m}$ flux density limits, however, mergers are not always required for the formation of DOGs. Massive discs can be red enough to satisfy the requisite infrared-optical color ratio for DOG selection, though are less bolometrically luminous.

The most luminous DOGs in Figure 8 tend to all be PL sources, consistent with observations (Dey et al. 2008). The isolated galaxies exhibit lower $24 \mu\text{m}$ flux densities, and are always bump DOGs. At lower flux densities, the SFR is correlated with the observed $24 \mu\text{m}$ flux density (C. Hayward et al., in prep.). As the contribution of AGN becomes non negligible, though, this relation breaks down (e.g., for most luminous sources). While the trends in Figure 8 are robust, we caution against interpreting the absolute values of the $24 \mu\text{m}$ flux density too literally. Rest frame mid-IR PAH features contribute to the observed F_{24} at $z \sim 2$. Modulating the assumed fraction of carbonaceous grains which emit the PAH template can shift the observed $24 \mu\text{m}$ flux density of a given galaxy. Changing the PAH fraction has the strongest relative effect on the lowest flux density galaxies, and at its limits (e.g., a PAH fraction of 0 or 1), can shift the observed flux density by up to a factor of $\sim 50\%$ (though the shift is less for more luminous sources).

To summarise, our models suggest that the most luminous DOGs (i.e., those with $F_{24} \gtrsim 300 \mu\text{Jy}$ at $z \approx 2$) likely result from mergers. In contrast, the less luminous DOGs can result from a wider range of (less extreme) conditions, perhaps even from secular evolution. Within this framework, there are a few salient points regarding the physical nature of DOGs that appear to be general to all DOGs selected at all flux density limits in our models.

First, in the absence of any merging activity, a DOG will never go through a PL phase. *Some* merging activity is necessary to produce the dust obscuration of UV radiation and/or AGN activity which drive the PL shape to the observed mid-IR spectra. Mergers are required to funnel sufficient gas to the central regions to suppress (or overwhelm) the stellar bump (and/or fuel the AGN). As such, PL DOGs constitute a relatively narrow class of galaxies, whereas bump DOGs are significantly more diverse as they are well represented by both mergers and non-mergers. This is seen explicitly in Figure 8.

Second, while it is not shown, there is a rough minimum galaxy mass necessary for forming DOGs. Nominally, galaxies with halos $M_{\text{bar}} \ll 5 \times 10^{11} M_{\odot}$ will not have the requisite gas supply to generate the starburst/AGN activity that drives the observed $24/R$ ratio. When mapping from baryonic masses to halo masses (e.g. Table 1), the halo masses are also consistent with the clustering measurements published by Brodwin et al. (2008). Moreover, the halo masses are consistent with the inferred halo masses of high-redshift galaxies of a comparable luminosity - that is, SMGs (Blain et al. 2004), and quasars (Croom et al. 2005; Lidz et al. 2006; Hopkins et al. 2007; Shen et al. 2007).

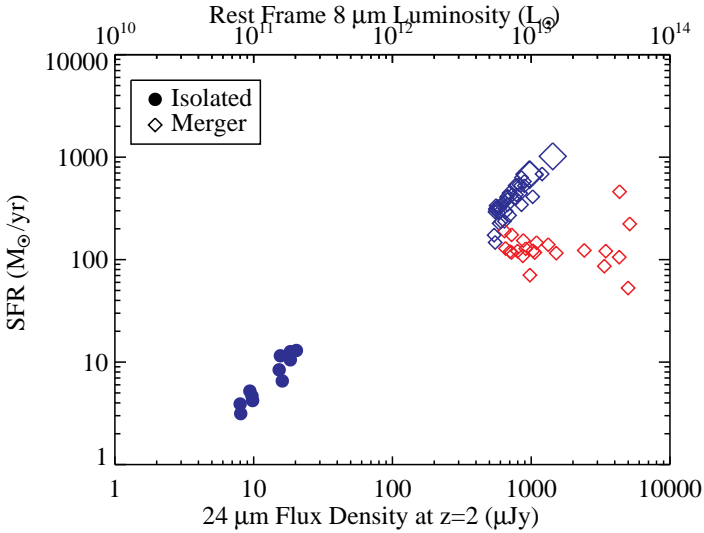


Figure 8. SFR versus 24 μm flux density for all snapshots of all model galaxies which qualify as DOGs ($24/R > 1000$, but with no 24 μm flux density limit). On the top axis, we show the rest-frame 8 μm luminosity. The different symbols denote whether the galaxies are mergers or isolated galaxies. The symbols which are double sized qualify both as DOGs, as well as $F_{850} > 5\text{mJy}$, though we defer discussion of the SMG-DOG overlap until § 5.1. There is a clear relation between the 24 μm flux density and SFR for the bump DOGs, though the contribution of AGN can muddy this for PL galaxies. Generally, the most luminous 24 μm sources require merging activity, and have PL mid-IR SEDs. As galaxies become less bright, they tend toward bump (star formation-dominated) galaxies, and are well described by non-mergers as well. The reader should note that the gap in between the mergers and isolated galaxies is artificial, and betrays the limited parameter space investigated in these models. This gap represents the transition from isolated galaxies dominating the bulk of the DOG population to mergers. A broader range of models run at more varied masses, merger orbits and gas fractions would fill this space in. It is moreover important to note that the flux densities on the abscissa are subject not only to the uncertainties present in this model (§ 2), but also the assumed redshift of $z=2.0$. As such, the normalisation of this trend should be taken with the appropriate caution.

5 RELATIONSHIP OF DOGS TO OTHER HIGH-REDSHIFT GALAXIES

5.1 Submillimetre Galaxies

A number of clues suggest an intimate link between high-redshift 850 μm -selected SMGs, and the DOG population (Dey et al. 2009). First, circumstantial evidence indicates physical similarities between SMGs and DOGs. SMGs are thought to form in massive starbursts which both observational and theoretical evidence imply may be merger-driven (e.g., Chapman et al. 2003; Tacconi et al. 2006, 2008; Baugh et al. 2005; Swinbank et al. 2008; Narayanan et al. 2009, 2010, though see Davé et al. (2009) for an alternative interpretation). Our model for DOG formation suggests that luminous DOGs, as well, are likely formed at the final stages of a merger (§ 4). Similarly, the inferred SFRs in SMGs and PL DOGs appear to both be extremely large ($\sim 700 - 1500 M_{\odot}\text{yr}^{-1}$; Swinbank et al. 2004; Kovács et al. 2006; Menéndez-Delmestre et al. 2007; Valiante et al. 2007; Dey et al. 2008; Bussmann et al. 2009; Desai et al. 2009). DOGs and SMGs cluster in similar mass halos (Brodwin et al. 2008), and tentative evidence suggests that they may contain somewhat similar mass stellar bulges (e.g. Swinbank et al. 2004; Borys et al.

2005; Bussmann et al. 2009; Michałowski et al. 2009). Second, Narayanan et al. (2010)’s merger-driven model for the formation of SMGs utilised similar merger models employed in this study. This overlap in modes of galaxy formation (a merger-based mode for both SMG and DOG formation) suggests not only a physical connection between SMGs and DOGs, but possibly an evolutionary one. Finally, and perhaps most convincingly, an analysis of the GOODS-N field by Pope et al. (2008) has found a bona fide overlap between the SMG and DOG populations: Namely, some $\sim 30\%$ of SMGs have $24/R$ colors consistent with DOG selection.

To assess the relationship between DOGs and SMGs, we now highlight the purple 850 μm flux density lightcurve overplotted in Figure 4. As the galaxies merge ($T \approx 0.65$ Gyr), radiation from the $\sim 1000\text{-}2000 M_{\odot}\text{yr}^{-1}$ starburst is intercepted by the cold ISM, and re-emitted by cold dust as submillimetre-wave emission (Groves et al. 2008; Jonsson et al. 2010; Narayanan et al. 2010). At the same time, diffuse dust in the galaxy heavily reddens the optical light, rendering the galaxy visible as a DOG. The model DOG10 would be classified as a bump galaxy at the exact same time as it would be visible as an SMG (Figure 4). The formal DOG phase follows after the SMG phase in this model, though we note that numerous models in Table 1 show an overlap of the two phases. After the SMG phase, the fiducial galaxy transitions from a bump DOG to a PL DOG. Because the SMG phase and DOG phase of the galaxy are both triggered by the merger, the phenomena are intimately related.

While Figure 4 is instructive as to a general sequence of events, it should not be construed to mean that all SMGs would be selected as DOGs, much less bump DOGs. Merger orbit, viewing angle, and mass can shift the exact timing and magnitude of events to make the overlap less straightforward. To show this, in Figure 9, we plot the 850 μm flux density from every snapshot in every model in Table 1, making two selection cuts: the galaxy has to either be classified as an SMG ($F_{850} > 5\text{mJy}$), or a DOG ($24/R > 1000$). We additionally note when the galaxies would be visible as bump sources, or PL DOGs. There is a significant overlap between the galaxy populations. A few features are apparent.

First, while there is overlap, many SMGs will not be selected as DOGs, and vice versa. Second, SMGs may be either bump or PL sources. The fact that some SMGs have bump mid-IR SEDs makes sense as the 850 μm flux which SMGs are selected on is powered by absorption of stellar light by cold clouds (Narayanan et al. 2010), and are generally thought to have their bolometric luminosity powered by star formation (Chapman et al. 2004; Alexander et al. 2005; Valiante et al. 2007; Pope et al. 2008; Younger et al. 2008a; Menéndez-Delmestre et al. 2009). That SMGs can also be PL DOGs may seem counterintuitive given that the dominant power source in SMGs is thought to be star formation. Recall, however, that some PL sources derive their mid-IR SED shapes from extremely heavy dust extinction at 5 μm , even while the AGN continuum does not dominate the mid-IR flux density. While the PL DOG phase is roughly contemporaneous with the rise in AGN continuum, they are not always exactly coincident in time.

SMGs will typically overlap with the more (24 μm) luminous DOGs. This owes to the fact that in our model, SMGs derive from massive mergers (see Figure 2 from Narayanan et al. 2010). The overlap of SMGs with high 24 μm flux density DOGs is apparent from Figure 8, where we highlight the symbols with double size which are galaxies which are selectable both as DOGs, as well as $F_{850} > 5\text{mJy}$ DOGs.

Finally, we caution that Figure 9 should not be interpreted as a

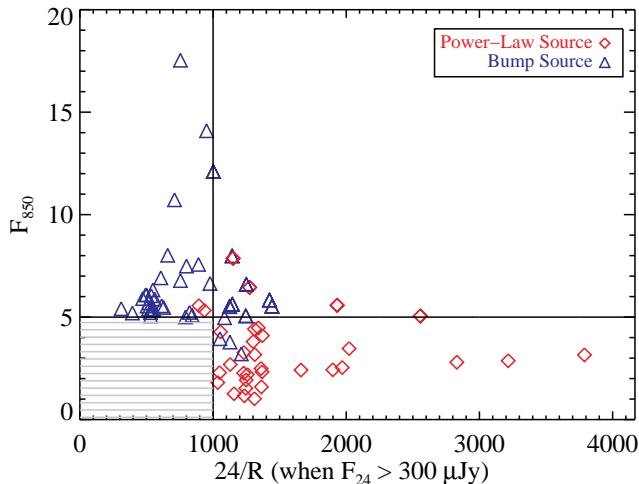


Figure 9. 850 μm flux density versus 24/R ratio for all 24 μm -selected galaxies in our model sample. Blue triangles show when the galaxies would be selected as bump DOGs, and red diamonds as PL DOGs. Only galaxies which are either SMGs or DOGs are plotted. The vertical and horizontal lines denote the DOG 24/R selection criteria and the SMG F_{850} selection criteria. While there is significant overlap between the SMG ($F_{850} > 5$ mJy) and DOG population, numerous DOGs are not detectable in the submillimetre, and vice-versa. It is important to recognise that the region of space where $24/R < 1000$ and $F_{850} < 5$ mJy (shown by the grey hatched region) is not populated by construction, as in this space galaxies are neither DOGs nor SMGs. In reality, a large number of galaxies reside in this portion of F_{850} -24/R space.

measure of the relative fractions of SMGs which are DOGs or vice versa. To construct those statistics will require a convolution of the SMG and DOG duty cycles with cosmological galaxy merger rates, a task deferred to a future study.

5.2 BzK Galaxies

The BzK selection criteria have been successfully used to find both star-forming and passively evolving galaxies at redshifts $1.4 \lesssim z \lesssim 2.5$ (e.g., Daddi et al. 2004). These samples overlap the DOG and SMG redshift ranges, and therefore provide an interesting comparison.

In Figure 10, we plot all DOGs in our simulation sample on the BzK color-color plot. In order to compare with Pope et al. (2008)’s analysis of GOODS-N DOGs (selected with $F_{24} > 100 \mu\text{Jy}$) in BzK space, we include all DOGs with $F_{24} > 100 \mu\text{Jy}$ at $z = 2$. We separate bump and PL DOGs, and overplot the rough criteria for star-forming galaxies ($(z - K)_{\text{AB}} - (B - z)_{\text{AB}} > -0.2$) devised by Daddi et al. (2004) (such that galaxies which lie above the line are star-forming BzK galaxies). Finally, we note the location of all galaxies in our simulation sample (whether or not they are DOGs) in $(z - K) - (B - z)$ space by dots.

Most DOGs in our sample are selected as BzK galaxies. This result is not surprising. Daddi et al. (2005) find that the majority of BzK galaxies in the GOODS-N field are 24 μm detected. In more direct comparison to these model results, Pope et al. (2008) find that nearly all DOGs in the GOODS-N field are selected as BzK galaxies. The results here are in good agreement with the dataset of Pope et al. (2008), spanning a similar range in $(B - z)$ and $(z - K)$ colors.

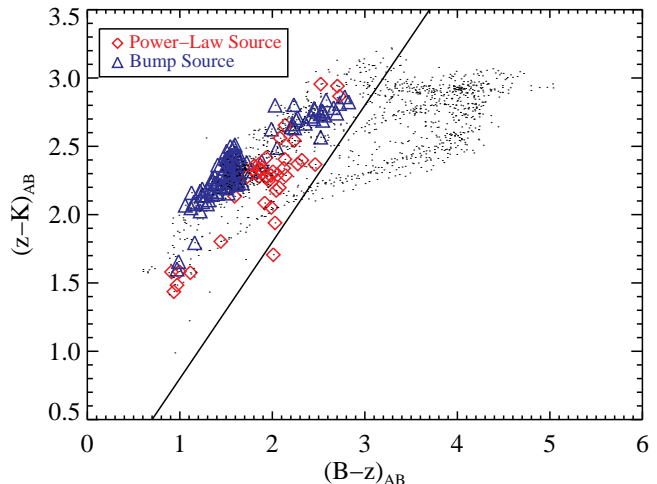


Figure 10. DOGs on BzK color-color plot. Bump and PL DOGs are denoted, and the selection criteria for star-forming galaxies ($(z - K)_{\text{AB}} - (B - z)_{\text{AB}} > -0.2$) is shown as a solid line (star-forming BzK galaxies lie above the line). We note the location of all galaxies in our simulation sample (whether or not they are DOGs) in $(z - K) - (B - z)$ space by dots. For the purposes of comparisons with observational data sets, DOGs in this plot are selected with $F_{24} > 100 \mu\text{Jy}$. Most model DOGs are selectable as BzK star-forming galaxies, consistent with studies of the overlap between GOODS-N BzK galaxies and DOGs (Pope et al. 2008).

There are two important caveats. First, while most DOGs can be selected as BzK galaxies, this does not mean that all BzK galaxies will be selected as DOGs. Observationally, Pope et al. (2008) find that only 12% of BzK galaxies are selectable as DOGs. Second, even though most DOGs fall into the star-forming region of the BzK color-color plot, they may not be detectable at optical wavelengths. Because the BzK criteria covers a broad range of star-forming galaxies, the DOG selection criteria selects a dusty subset of the BzK ’s.

6 OBSERVATIONAL CONSEQUENCES OF THE MODEL

In order to assess the validity of our models, we compare the simulated and observed SEDs. We then make testable predictions of these models, and provide analysis tools via public SED templates. When comparing to observations, we focus primarily on the dynamic range of fluxes and color ratios. Matching the observed distributions (e.g., luminosity functions, color distributions) requires cosmological galaxy formation simulations, and will be presented in forthcoming work.

6.1 Comparisons to Observations: Optical-mm Wave SED

Observed SEDs of DOGs with spectroscopic redshifts have been compiled by Bussmann et al. (2009, in prep). In Figure 11, we present the model SEDs for four merger-driven DOGs which span the (mass) range of galaxies which form $F_{24} > 300 \mu\text{Jy}$ DOGs (DOG1, DOG4, DOG7 and DOG10) and sample the full mass ratios of simulated mergers. We note that this is a simple mass (and mass ratio) scaling in simulated mergers, but aside from this, the initialisation of each merger (including galaxy orbit) remains identical. The SED is modeled for every snapshot while the galaxy is a

DOG (above $F_{24} > 300 \mu\text{Jy}$), and is averaged over all camera angles. The black line represents the time and camera-averaged SED, and the blue shaded region denotes the 1σ temporal dispersion for each model. The SED is modeled to be at $z=2.0$. The red squares show the mean of all data in the Bussmann et al. sample for DOGs above $F_{24} > 300 \mu\text{Jy}$ within the redshift range $1.75 < z < 2.25$, and the error bars denote the propagated errors. In order to more accurately compare with the Bussmann et al. sample, we performed a Monte Carlo drawing of the galaxies in our simulation sample that forced our final sample to be comprised of 50% bump DOGs and 50% PL DOGs in the composite SED. This is comparable to the breakdown of mid-IR SED types in the observational dataset of Bussmann et al. We note, however, that simply including all DOG snapshots in our simulation sample makes little difference on the final composite SED. We additionally include template SEDs for local galaxies Mrk 231 (Armus et al. 2007; Chary & Elbaz 2001, R. Chary, private communication), and Arp 220 (Rieke et al. 2009), each scaled to match the Bussmann et al. MIPS 24 μm point and redshifted to $z=2.0$.

Generally, there is a reasonable match between the observed and modeled SEDs. The correspondence between the simulated optical, NIR and FIR SEDs, and those observed in DOGs implies that the models presented here have a similar UV flux from newly formed stars, stellar mass, and dust obscuration column as DOGs in nature. There are relatively minor discrepancies in the observed-frame NIR and mid-IR. The Mrk 231 and Arp 220 templates both have weaknesses in matching the observed data. The Arp 220 template overpredicts both the rest-frame optical-NIR and FIR flux densities. Similarly, the Mrk 231 SED underpredicts the rest-frame UV substantially. Given the relatively improved match between these models and the observed data points (as opposed to the local templates), we provide the model SEDs as templates in § 6.3.

Figure 12 shows where the simulated galaxies fall on an IRAC color-color diagram. Here, we have taken our simulated galaxies, and redshifted them between $z=1.5$ to 2.4 incrementally (in steps of $\Delta z=0.1$), and plotted all galaxies with a $24/R$ ratio > 1000 , and $F_{24} > 300 \mu\text{Jy}$. The dots show the galaxies which have $F_{24} > 300 \mu\text{Jy}$, but do not have the requisite $24/R$ ratio to be selected as a DOG. The PL DOGs show redder colors than the bump DOGs, which in turn are redder (in $5.8/3.6$) than the non-DOG $24\mu\text{m}$ sources. The simulated colors of all models lie roughly in the same region as the observations (Desai et al. 2009; Lacy et al. 2004), but span a smaller dynamic range. The solid lines enclose the region noted by Lacy et al. (2004) to typically contain AGN. Both observed DOGs (Desai et al. 2009) and these models tend to fall primarily in the Lacy et al. (2004) AGN-wedge. While indeed DOGs powered by AGN fall into the AGN-wedge, many starburst-dominated galaxies appear to as well.

6.2 Testable Predictions

Our modeling suggests that the bright DOGs ($F_{24} > 300 \mu\text{Jy}$ at $z=2$) are the result of mergers and represent a phase of massive galaxy evolution following a sub-mm bright phase. If true, the models can be used to predict observational tests of this scenario. We note that these tests do not apply to the fainter DOGs, which are a more diverse population.

6.2.1 The Physical Masses of DOGs and Their Relation to SMGs

In Figure 13, we plot the range of black hole, stellar, dark matter, and H_2 masses for all galaxies in our simulated sample at times they may be a DOG, discriminating both bump and PL DOGs ($F_{24} > 300 \mu\text{Jy}$). This prediction is made for galaxies that would be selected as DOGs between a redshift range of $z=1.6-2.4$. We additionally show the same prediction for all galaxies in our simulations which would be selected as SMGs (with $F_{850} > 5 \text{ mJy}$). The black hole, stellar, and halo masses are extracted directly from the hydrodynamic simulations. We note that the halo masses are predicted by construction as the mass of the simulated galaxies is set by the initial halo mass. While the SPH simulations do not explicitly follow the H_2 molecular gas, we infer its mass by considering all of the dense, star-forming gas to be neutral, and extracting the H_2/HI fraction utilising the Blitz & Rosolowsky (2006) interstellar pressure-based prescription (Narayanan et al. 2009).

Because we are considering a $F_{24} > 300 \mu\text{Jy}$ flux density limit, all of the DOGs in this plot formed from mergers. Mergers produce the bulk ($\sim 90\%$) of their stellar mass prior to the final merging (Narayanan et al. 2008, 2009, T.J. Cox et al. 2009, submitted). Consequently, DOGs which form at the final coalescence of a merger will typically have already formed the bulk of their stellar mass. As such, the bump DOGs and PL DOGs in our simulations tend to have relatively large stellar masses, $M_* \gtrsim 10^{11}$, comparable to observations (Lonsdale et al. 2009; Bussmann et al. 2009). Because similar types of galaxies form SMGs and bright ($F_{24} > 300 \mu\text{Jy}$) DOGs (e.g. massive mergers), there is substantial overlap between the physical properties of bright DOGs and SMGs. Generally, only the halo masses are well-constrained for DOGs. As such, the remaining physical properties (stellar, BH, gas masses) shown in Figure 13 serve as a prediction.

The growth story for black holes is markedly different from that of the stars. Black holes in mergers undergo the bulk of their growth during the final merging (see, e.g., Figure 5 from Narayanan et al. 2008). As such, because the PL phase tends to follow the bump phase in these high-redshift merger models, on average, the black holes in PL DOGs will be larger than those in bump DOGs.

We can utilise this growth history of stellar and black hole masses in mergers to provide a test for our evolutionary model for mergers to transition from an SMG phase to a PL DOG phase (e.g., Figure 4). Merger remnants, in our simulations, lie on the $M_{\text{BH}}-M_{\text{bulge}}$ relation owing to the termination of the starburst event by AGN feedback, and self-regulation of black hole growth (Di Matteo et al. 2005; Robertson et al. 2006; Hopkins et al. 2007; Younger et al. 2008b; Li et al. 2007). Because the black holes grow substantially during the final coalescence of a merger, one might expect that the black holes in SMGs will be smaller, on average than those in PL DOGs if SMGs are to evolve into PL DOGs as these models suggest (Figure 4). In contrast, their stellar masses will be roughly comparable as the stellar masses are already in place at final merging.

To test this, we compare the location of all bright SMGs and bright ($F_{24} > 1 \text{ mJy}$) DOGs in our simulation sample on the $M_{\text{BH}}-M_{\text{bulge}}$ relation (Figure 14). We bin the SMGs into average ($F_{850} > 5 \text{ mJy}$) and bright ($F_{850} > 10 \text{ mJy}$) bins. The extremely bright ($F_{850} > 10 \text{ mJy}$) SMGs constitute a cleaner test as they are always galaxies at the peak of their starburst, whereas lower flux density sources (e.g., $F_{850} \approx 5 \text{ mJy}$) SMGs can be either lower mass galaxies at the peak of their starburst, or more luminous galaxies both pre and post-starburst (Narayanan et al. 2009, 2010). Never-

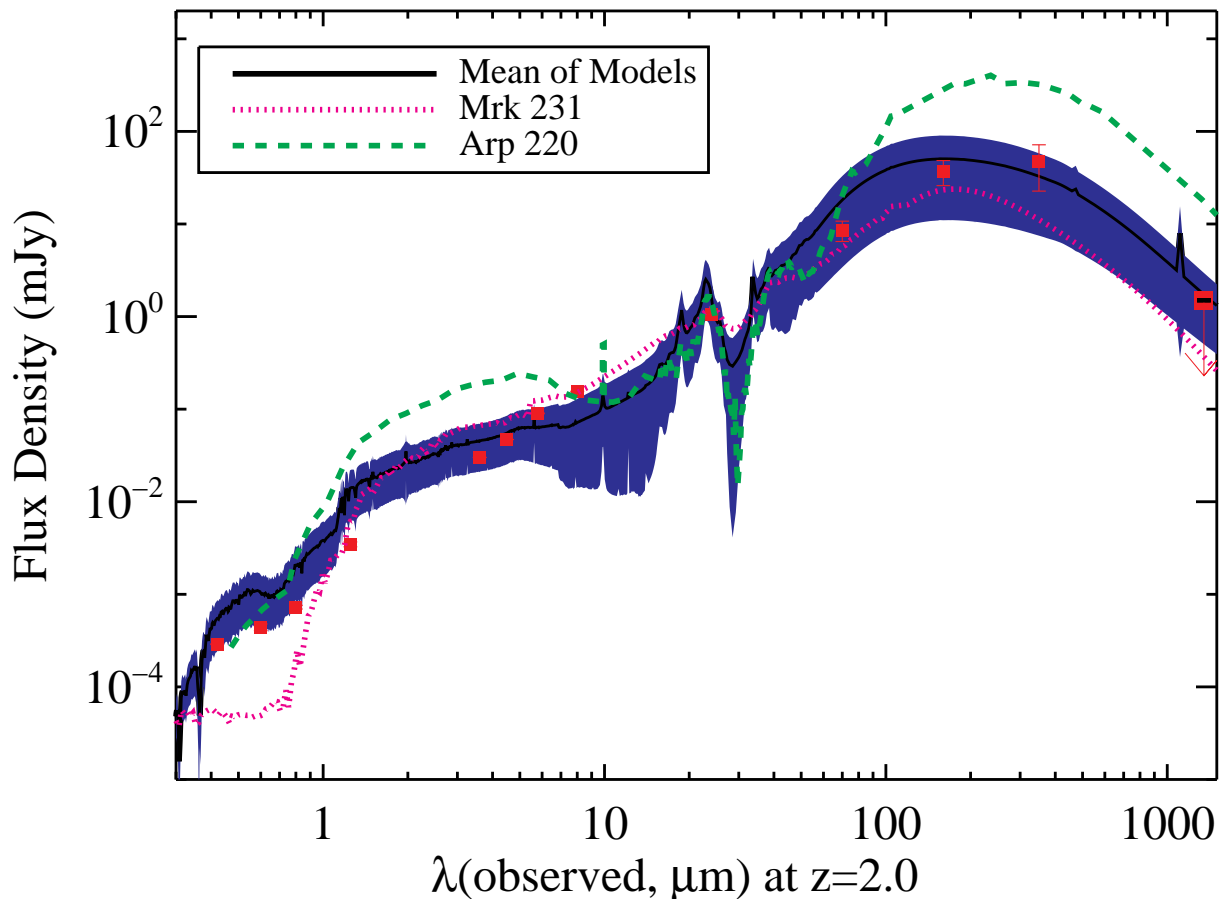


Figure 11. Simulated SEDs redshifted to $z=2$ for model galaxies. The SED was calculated for all snapshots that satisfied the DOG selection criteria ($24/R > 1000$, $F_{24} > 300 \mu\text{Jy}$) for four model galaxies which sample the full mass and merger mass ratio range of our simulation sample (DOGs 1, 4, 7 and 10): The 1σ dispersion amongst these snapshots is shown by the blue shaded region, and the mean by the black solid lines. The model SED is compared to the compiled observational data points (red) by Bussmann et al. (in prep) for all $F_{24} > 300 \mu\text{Jy}$ DOGs with spectroscopic redshifts $1.75 < z < 2.25$. If error bars are not shown, it is because they are smaller than the symbol representing the data point. In order to best compare with the Bussmann et al. sample, we did a Monte Carlo sampling of our model SEDs that enforced that we had 50% bump DOGs and 50% PL DOGs in the sample, comparable to the relative breakdown of mid-IR SED types in the Bussmann et al. sample. The magenta dotted lines and green dashed lines are template SEDs for local galaxies Mrk 231 and Arp 220, scaled in flux density to match the observed Bussmann et al. $24 \mu\text{m}$ data point, and scaled to $z=2.0$. The modeled SED and observed data generally correspond well, suggesting a reasonable match between the modeled stellar mass and flux and obscuring dust columns and temperature in the modeled galaxies and DOGs in nature. That said, the modeled mid-IR SED shows some disagreement with the observed IRAC points (especially at $8 \mu\text{m}$). Neither the Mrk 231 and Arp 220 templates provide good matches to the observed data.

theless, we include lower flux density ($F_{850} > 5 \text{ mJy}$) SMGs for the purposes of comparison with existing data sets.

Figure 14 shows a direct prediction for our model. Most SMGs will lie below the present-day $M_{\text{BH}}-M_{\text{bulge}}$ relation as their black holes have significant growth they will undergo throughout the remainder of the merger (e.g., Alexander et al. 2008). They typically have stellar masses ranging from $10^{11} - 10^{12} M_{\odot}$, with the more common SMGs tending toward the lower end of this mass range⁵. Bright PL DOGs, which occur contemporaneously with or later than SMGs in a merger’s evolution (e.g., Figure 4) will range

from falling below the present-day $M_{\text{BH}}-M_{\text{bulge}}$ relation, to directly on/above it.

6.2.2 T_{Dust} of DOGs

Forthcoming facilities which probe both sides of the peak of the SED of DOGs (e.g., *Herschel*, ALMA) will place strong constraints on the effective dust temperature. These dust temperatures will serve as a test for the predicted SEDs of DOGs from our models.

In Figure 15, we plot the predicted dust temperature of our model DOGs as a function of their FIR luminosity ($40\text{-}1000 \mu\text{m}$). The dust temperature is derived by converting the rest-frame wavelength of the SED peak to a temperature (using Wien’s displacement law), and is calculated for every snapshot where $24/R > 1000$

⁵ Indeed comparison to the compilation of SMGs by Alexander et al. (2008) (the blue cross) shows that the average observed SMG is more similar to our SMG models which form lower mass galaxies.

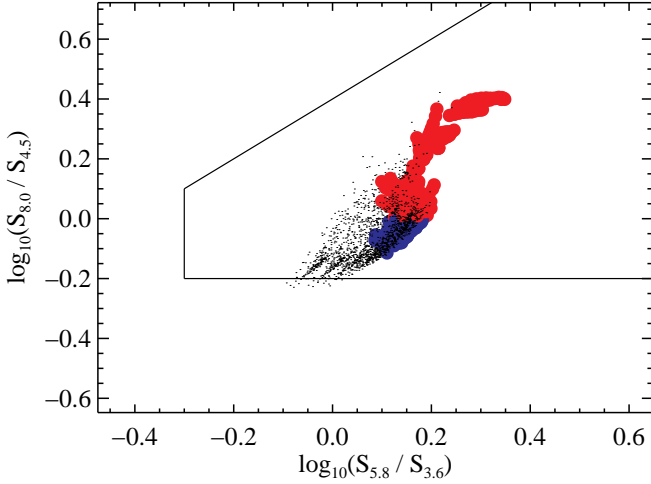


Figure 12. Mid-IR color-color plot for all model galaxies which would be selected above a $24\ \mu\text{m} > 300\ \mu\text{Jy}$ flux density cut. DOGs are shown as colored points, with bump DOGs as blue symbols and PL DOGs as red symbols. Black dots represent $24\ \mu\text{m}$ selected galaxies which do not qualify as DOGs. The model galaxies are incrementally redshifted from $z=1.5-2.4$, and plotted when they are selectable as DOGs. The solid lines enclose the typical region of color-color space occupied by AGN-dominated galaxies as found by Lacy et al. (2004). The locus of PL DOGs lie in the top-right region of these plots (e.g., Lacy et al. 2004) owing to their rising mid-IR SEDs. The model DOGs lie roughly in the same region of the mid-IR as observed DOGs (Desai et al. 2009), though span a smaller dynamic range.

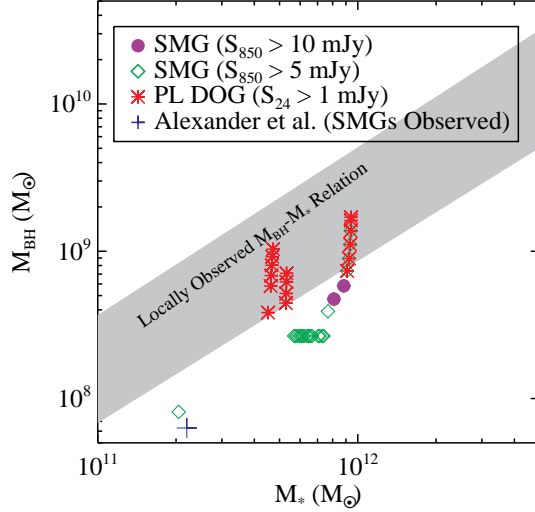


Figure 14. Bright ($F_{24} > 1\ \text{mJy}$) PL DOGs and SMGs (in two flux density bins) on the present day $M_{\text{BH}}-M_{\text{bulge}}$ relation. The purple circles denote bright SMGs, the green diamonds the average SMGs, the blue cross the results from observed SMGs by Alexander et al. (2008), the red asterisks bright DOGs, and the grey shaded region the locally observed $M_{\text{BH}}-M_{\text{bulge}}$ relation (including dispersion). In our model, SMGs typically precede the PL DOG phase in mergers. During this time, while the stellar mass is roughly in place, the black holes undergo significant growth, placing SMGs and PL DOGs at different locations on the $M_{\text{BH}}-M_{\text{bulge}}$ relation. Observations pinpointing the location of SMGs and PL DOGs on the $M_{\text{BH}}-M_{\text{bulge}}$ relation will serve as a test for our model connecting SMGs and DOGs.

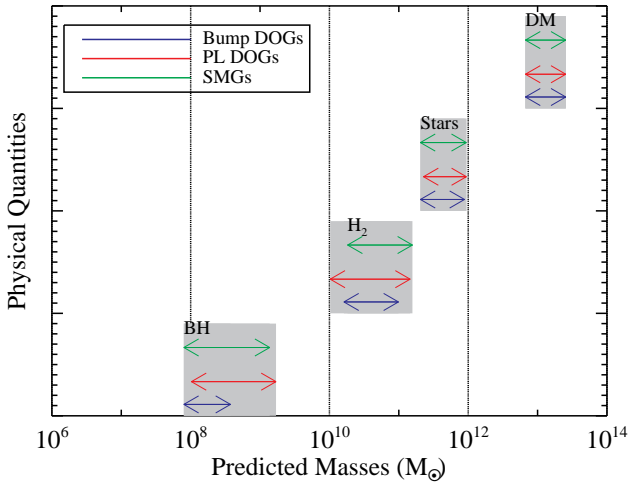


Figure 13. Predicted range of physical properties of DOGs and SMGs ($F_{24} > 5\ \text{mJy}$). Shown are black hole masses, H_2 masses, stellar masses and halo masses for galaxies which would be selected as DOGs between redshifts $z=1.6$ and 2.4 . Blue arrows denote bump DOGs and red arrows, PL DOGs. The vertical lines are simply to guide the eye to the axes. DOGs are relatively massive galaxies, with PL DOGs tending toward the higher mass end of the mass distribution. It is important to note that owing to relative abundances, most observed DOGs are likely to occupy the lower end of the predicted ranges. Because similar types of galaxy (mergers) represent SMGs and bright DOGs, they share an overlap in physical properties. Because only halo masses are known for DOGs, the remaining physical properties serve as a strong testable prediction of these models.

and $F_{24} > 100\ \mu\text{Jy}$ (we utilise the lower flux density limit for completeness). For reference, we show all times when the model galaxies would be visible as SMGs ($F_{850} > 5\ \text{mJy}$ as well). While deriving T_{dust} from the full SED is a different approach than that typically used by observers (who fit the observed data with SEDs varying T_{dust} and the dust spectral index, β , which are degenerate with one another), we prefer this method: Utilising the entire model SED avoids any assumptions about β , which is observed to fall within a relatively large range of $\beta = 1 - 2$ for $z \sim 2$ SMGs and DOGs (Kovács et al. 2006; Bussmann et al. 2009).

For star-forming galaxies (including bump galaxies and SMGs), there is a general trend for brighter sources to have hotter dust temperatures (which is largely a selection effect for galaxies selected for cold dust emission). PL DOGs typically have hotter dust temperatures than bump DOGs and SMGs. These features are consistent with observations of both high redshift galaxies (e.g., Bussmann et al. 2009; Casey et al. 2009; Younger et al. 2009; Kovács et al. 2006, 2010) and local ULIRGs (e.g., Sanders & Mirabel 1996). For example, Figure 15 also shows $z \sim 2$ bump ULIRGs from Younger et al. (2009) and Kovács et al. (2010), SMGs from Kovács et al. (2006), and two lower limits from PL DOGs from Bussmann et al. (2009) as black circles, purple triangles, and cyan diamonds, respectively. The ULIRGs from the Younger et al. (2009) sample were selected based on their stellar bump (Huang et al. 2009), and are thus bump galaxies. For the bump ULIRGs of Kovács et al. (2010), we divided the luminosity by a factor of 2 to convert from L_{IR} to $L_{40-1000}$, based on the approximate conversion for Mrk 231. Both the bump ULIRGs and SMGs span a similar range in $T_{\text{dust}}-L_{\text{IR}}$ space as these simulations. Dust temperature determinations for bright PL DOGs will provide

a more stringent test of these models as they are expected to show a larger range of dust temperatures than either SMGs or bump galaxies.

6.2.3 The CO Line Widths from DOGs

Narayanan et al. (2008, 2009) found that CO traces the global kinematics of a galaxy. The CO line widths can constrain the masses and dynamical states of galaxies which form DOGs, and thus constitute a testable prediction of these models. For example, while in an isolated disc galaxy, the line width is reflective of the virial velocity of the galaxy. In a merger, the CO linewidths may increase by a factor $\sqrt{2} - 2$, owing to multiple galaxies being in the observational beam and the temporary disruption of molecular discs. In this picture, galaxies which owe their origin to mergers will exhibit larger CO line widths than secularly evolving galaxies.

In order to examine the predicted CO line widths from DOGs, we employ TURTLEBEACH, a 3D non-local thermodynamic equilibrium molecular line radiative transfer code (Narayanan et al. 2006, 2008, 2009). TURTLEBEACH is an iterative Monte Carlo code which considers both radiative and collisional processes in determining the molecular excitation (and, hence, source functions), and assumes statistical equilibrium in the levels (Narayanan et al. 2008, 2009). For galaxy-scale simulations, we implement a subgrid procedure for including a mass spectrum of giant molecular clouds as singular isothermal spheres, which follow the Galactic mass spectrum (Rosolowsky 2005) and mass-radius relationship (e.g., Solomon et al. 1987). Once the level populations have converged from the Monte Carlo code, the equation of radiative transfer is integrated through the grid to build the emergent spectrum.

In Figure 16, we plot the range of CO (J=3-2) FWHM for all model galaxies in Table 1 when they classify as a luminous ($F_{24} > 300 \mu\text{Jy}$) DOG at $z=2$. As a comparison, we plot the CO FWHM from the same model galaxies when they would classify as an SMG ($F_{850} > 5 \text{ mJy}$). The line widths are viewing angle dependent, and, as such, we include the line widths from 100 random sightlines for each model galaxy. The ranges are plotted in histogram form, with each random sightline of each snapshot qualifying as an individual galaxy for the histogram. It is crucial to note that the histogram does *not* represent a probability distribution function. Rather, the ordinate values are meaningless as the galaxies are not drawn from a cosmological simulation representing true mass functions and merger rates. The robust quantity to take from Figure 16 is the *range* of predicted CO line widths for DOGs and SMGs.

The line widths from DOGs show a large range, from $\sim 100 \text{ km s}^{-1}$ to $> 1500 \text{ km s}^{-1}$. This owes to the fact that both relatively minor mergers (e.g., DOG9) as well as massive major mergers (e.g., DOG1) form DOGs. The former are in a relatively dynamically relaxed state, and can be viewed along some viewing angles in a face-on configuration, causing small line widths. The latter almost always have relatively large line widths. The CO line widths from SMGs, in contrast, are typically quite large, ranging from $\sim 500\text{--}1500 \text{ km s}^{-1}$. This owes to their origin in massive major mergers (Narayanan et al. 2010). Hence, DOGs which may be in a disc-like configuration at times, are expected to espouse a much larger range of CO line widths than SMGs. Tentative observational evidence suggests that this may indeed be the case (Greve et al. 2005; Tacconi et al. 2006, 2008; Yan et al. 2010).

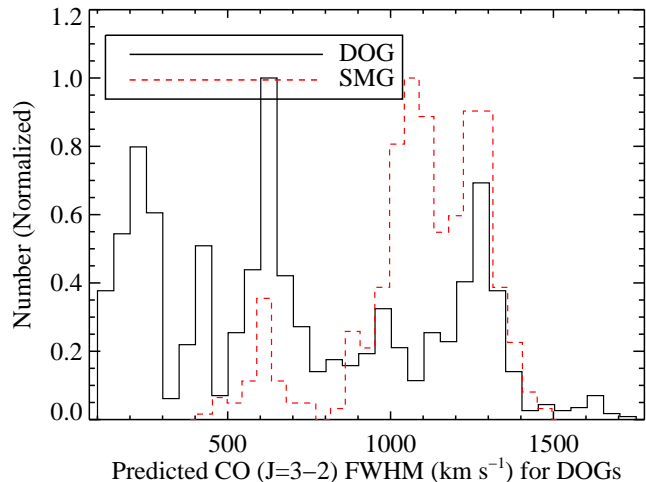


Figure 16. Predicted CO (J=3-2) line widths (FWHM) for model galaxies when they qualify as DOGs and/or SMGs. The latter galaxy population is selected via a submillimetre flux density cut, $F_{850} > 5 \text{ mJy}$. Line widths in galaxies are a function of their mass and dynamical state. Because DOGs can be either minor mergers (which may maintain a disc-like gas configuration), or major mergers (which are dynamically hot), the CO line widths span a large range (FWHM $\sim 100\text{--}1500 \text{ km s}^{-1}$). In contrast, because our modeled SMGs all owe their origin to massive mergers, they typically have large CO line widths (Narayanan et al. 2009). (See text for further details.) It is important to note that the histograms are not true distributions, but rather simply the range of expected CO line widths from these galaxy populations. Because line width roughly scales with mass, the average galaxy will have line widths toward the lower end of the predicted ranges.

6.3 Analysis Tools: IR SED Templates

We provide public SED templates of $z \sim 2$ DOGs both to serve as a testable prediction for these models, as well as an analysis tool for forthcoming *JWST*, *Herschel*, 1.1mm and ALMA observations. The templates are at model spectral resolution covering 968 wavelengths between approximately 0.3 micron and 3 mm. The SEDs are provided at $z=2.0$, the mean redshift for DOGs, and are calculated utilising every model in the simulation sample. The templates are provided as a function of total infrared luminosity (1-1000 μm). The templates as well as an IDL script to read them in (and redshift them to arbitrary redshifts) may be found at http://www.cfa.harvard.edu/~dnarayan/DOG_SED_Templates.html.

7 DISCUSSION

7.1 The Role of DOGs in Galaxy Evolution

The models presented here suggest that the bright DOGs are the result of mergers, whereas the fainter DOGs can have diverse origins. At the high flux density end ($F_{24} \gtrsim 300 \mu\text{Jy}$ at $z \approx 2$), DOGs represent the coalescence phase of massive, gas rich galaxy mergers residing in large ($M_{\text{DM}} \approx 10^{13} M_{\odot}$) halos. Bolometrically, these galaxies are amongst the most luminous at $z \sim 2$, and form stars at rates of $\text{SFR} \gtrsim 500 M_{\odot} \text{ yr}^{-1}$. Forming bulges with masses a few $\times 10^{11} M_{\odot}$ during the course of their mergers, these galaxies likely are precursors to massive present-day spheroids. These merger-driven DOGs share an intimate link with SMGs, and represent objects actively transitioning between having their IR luminos-

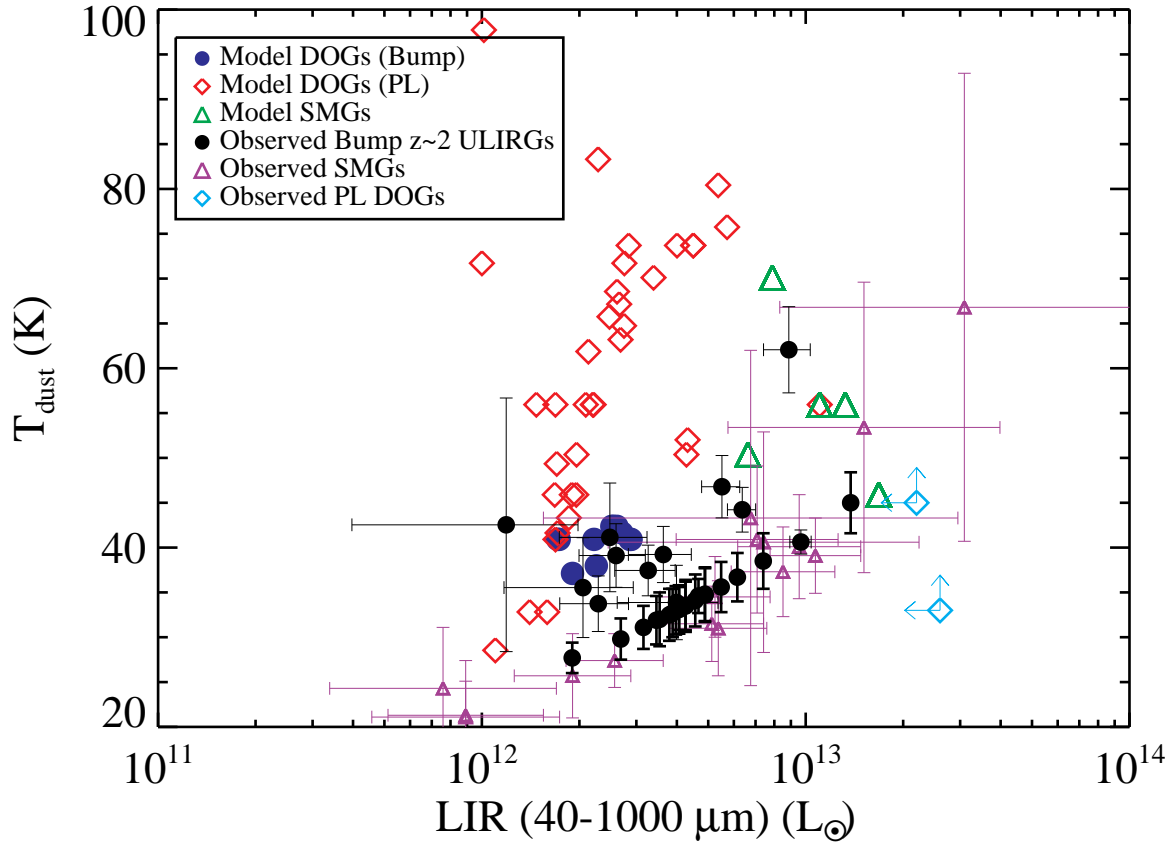


Figure 15. Predicted T_{dust} for DOGs above $F_{24} > 100 \mu\text{Jy}$ and SMGs with $F_{850} > 5 \text{ mJy}$ as a function of $L_{\text{IR}}(40\text{-}1000 \mu\text{m})$. The simulated T_{dust} is calculated via the peak of the sightline averaged SED. There is a general trend for brighter DOGs to exhibit hotter dust temperatures. PL DOGs have hotter dust temperatures than bump DOGs, as well as SMGs. For comparison, we show observational data points from Younger et al. (2009); Kovács et al. (2010), Kovács et al. (2006) and Bussmann et al. (2009) which represent 1 mm-selected $z \sim 2$ bump ULIRGs, $z \sim 2$ SMGs, and PL DOGs (lower limits) respectively. There is a reasonable agreement with the high- z observations and these simulations.

ity dominated by reprocessed stellar radiation to being dominated by a dust-enshrouded AGN. These massive mergers provide a natural avenue for supermassive black hole growth, fueling the growth of $\sim 10^9 M_{\odot}$ black holes.

The bright DOGs ($F_{24} > 300 \mu\text{Jy}$) typically are undergoing either a starburst (here, roughly $\gtrsim 500 M_{\odot} \text{yr}^{-1}$) or contain an actively accreting AGN ($\dot{M}_{\text{BH}} \gtrsim 0.5 M_{\odot} \text{yr}^{-1}$). These phenomena are most easily achieved via mergers. As was seen in Figure 8, 1:1 mergers are not necessary, and more “minor” mergers (here, 1:3) can form bright DOGs. Given the increasing relative number densities of minor mergers (e.g., Fakhouri & Ma 2008; Hopkins et al. 2009), it may be that these sorts of mergers dominate bright DOG formation. It is interesting to note that the higher mass-ratio mergers (e.g., 1:10) are not dissimilar qualitatively from galaxies which are accreting massive amounts of cold gas from their parent halo at $z \sim 2$ (e.g., “Stream Fed Galaxies”; Kereš et al. 2005; Birnboim et al. 2007; Dekel et al. 2008, 2009; Kereš et al. 2009).

At lower ($24 \mu\text{m}$) flux densities ($F_{24} \lesssim 100 \mu\text{Jy}$), DOGs can result from either galaxy mergers or galaxies undergoing secular evolution, not in any active stage of heightened star formation or AGN activity. These galaxies tend to have lower SFRs ($\sim 50\text{-}100$

$M_{\odot} \text{yr}^{-1}$), though are of comparable mass as their merging counterparts. In order to be selected as DOGs, these galaxies must be viewed in an edge-on configuration which maximizes the dust reddening. These galaxies may have overlap with the high redshift BzK population, and (in these simulations) always have their infrared luminosity dominated by star formation. DOGs form a continuum, then, of galaxies, parameterised by their $24 \mu\text{m}$ luminosity. As such, there is, of course, overlap between merging and non-merging DOG populations in this sequence.

Quantifying the exact number statistics of types of galaxies (e.g galaxy mass, merger mass ratio) in a given luminosity bin requires convolving light curves with cosmological galaxy merger rates, a task that is outside the scope of this paper. That said, these model results do point us toward some understanding of the physical form of DOGs at various luminosities. Figure 8 demonstrates that mergers dominate the high flux density end, whereas isolated disc galaxies contribute to the fainter population. Generically, we can say that the lower flux density DOGs, commonly identified in the deep, narrow field surveys, are likely to be a different breed than higher flux density DOGs which are typically uncovered by the wide-area *Spitzer* surveys.

The idea that DOGs have luminosity-dependent physical

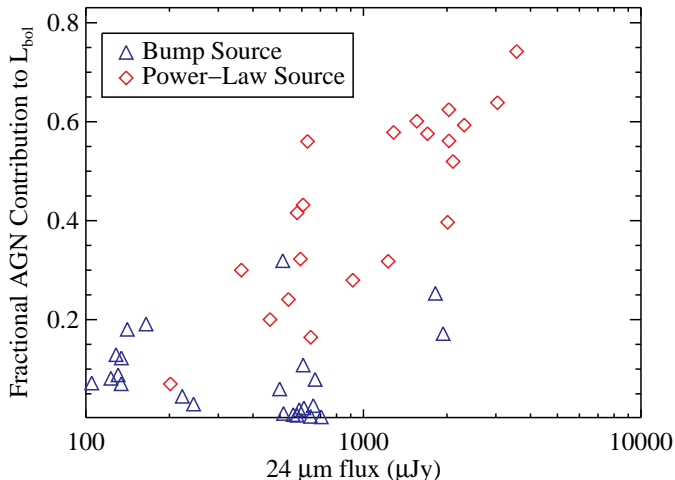


Figure 17. Fractional AGN contribution to bolometric luminosity for DOGs (above $F_{24} > 100 \mu\text{Jy}$) versus $24 \mu\text{m}$ flux density. Generally, more luminous DOGs tend to have larger AGN contributions to their total luminosity.

properties has already been seen in observational data sets. For example, there is some evidence that more luminous DOGs are more likely to harbor AGN. D08 noted that at increasing $24 \mu\text{m}$ flux densities, a larger fraction of galaxies are X-ray detected and have PL mid-IR SEDs. Similarly, a number of studies have shown that luminous DOGs ($F_{24} \gtrsim 500 \mu\text{Jy}$) may be Compton thick and contain obscured AGN (Fiore et al. 2008, 2009; Georgantopoulos et al. 2009; Sacchi et al. 2009). In our simulations, we see that brighter sources have increasing contribution to the bolometric luminosity by AGN (Figure 17). While assessing whether or not these AGN are Compton thick is outside the scope of this work, we can make some crude estimates along these lines. If we assume that the molecular ISM in our simulations is uniformly distributed in the nuclear regions (as is thought to be the case for local mergers; Downes & Solomon 1998), and not terribly clumpy, then we find some sightlines towards the nucleus may be marginally Compton thick ($N_{\text{H}} \sim 10^{24} \text{ cm}^{-2}$). However, a full investigation assessing the sightline dependence of column densities as well as the assumptions regarding the cold-phase clumping will be necessary to fully address whether these simulated DOGs are Compton thick.

Further evidence for luminosity-dependent physical properties in DOGs comes from Melbourne et al. (2009), who found an increasing concentration and decreasing half-light radius with increasing $24 \mu\text{m}$ flux density in DOGs. Finally, Brodwin et al. (2008) found that DOGs exhibit luminosity-dependent clustering, such that the most luminous DOGs in their sample ($F_{24} > 600 \mu\text{Jy}$) tend to reside in $\sim 10^{13} M_{\odot}$ halos, while less luminous ($F_{24} > 300 \mu\text{Jy}$) DOGs are associated with lower mass $M_{\text{DM}} \approx 2 \times 10^{12} M_{\odot}$ halos. All of these are generally consistent with our picture for more luminous DOGs to be represented by high-redshift mergers, and less luminous DOGs displaying less star formation and AGN activity (Figure 17).

8 SUMMARY AND CONCLUSIONS

Utilising a combination of polychromatic radiative transfer calculations and hydrodynamic simulations of high-redshift galaxy evo-

lution, we have formulated a physical model for the formation and evolution of $z \sim 2$ Dust-Obscured Galaxies. We have utilised the very similar models as those employed in previous studies aimed at investigating the formation and evolution of a similar class of $z \sim 2$ ULIRGs: the Submillimetre Galaxy population.

While the uncertainty in the models is dominated by small-scale physics which is unresolved by the simulations, our methodology allows us to make the following general conclusions regarding the origin of DOGs, and their relationship to other high- z ULIRGs:

- DOGs are a diverse class of galaxies, ranging from secularly evolving star-forming disc galaxies (forming stars at $\sim 50\text{-}100 M_{\odot} \text{ yr}^{-1}$) to extreme gas-rich galaxy mergers forming stars at $\gtrsim 1000 M_{\odot} \text{ yr}^{-1}$.
- The most luminous DOGs ($F_{24} \gtrsim 300 \mu\text{Jy}$) are well represented by mergers of massive ($M_{\text{DM}} \approx 5 \times 10^{12} - 10^{13} M_{\odot}$) galaxies. These galaxies are actively transitioning from being starburst dominated to being AGN dominated. At decreasing $24 \mu\text{m}$ flux densities ($F_{24} \lesssim 100 \mu\text{Jy}$), DOGs may either be galaxy mergers, or secularly evolving disc galaxies with more modest ($\sim 50\text{-}100 M_{\odot} \text{ yr}^{-1}$) SFRs.
- Luminous, merger-driven DOGs naturally transition from having a bump-like mid-IR SED to a power-law (PL) shape, as the dominant power source transitions from star formation to the central AGN. That said, there is an overlap period where star-formation dominated sources can appear as PL galaxies.
- The most luminous DOGs assemble both significant stellar masses ($M_{\star} \approx 10^{11} M_{\odot}$), as well as contribute toward the growth of supermassive ($M_{\text{BH}} \approx 10^9 M_{\odot}$) black holes.
- Merger-driven DOGs overlap with the $z \sim 2$ Submillimetre Galaxy population. SMGs generally represent the earlier, starburst-dominated phase of the DOGs evolution. This can be tested via the location of SMGs and DOGs on the $M_{\text{BH}}\text{-}M_{\text{bulge}}$ relation.

In advance of *Herschel*, *JWST* and ALMA, we provide the following testable predictions for our model of DOG formation:

- We quantify the expected range of black hole, H_2 , stellar, and halo masses for luminous ($F_{24} > 300 \mu\text{Jy}$) DOGs as well as SMGs.
- We provide dust temperatures for DOGs selected at various $24 \mu\text{m}$ flux density limits.
- We detail the location of SMGs and bright ($F_{24} > 1 \text{ mJy}$) DOGs on the $M_{\text{BH}}\text{-}M_{\text{bulge}}$ relation as a test for the modeled evolutionary scenario that SMGs evolve into PL DOGs.
- We provide a prediction for the CO line widths from DOGs, and suggest that they will be of order the largest observed line widths at high redshift, comparable to $z \sim 2$ SMGs.

Finally, we provide model SED templates for $z=2$ DOGs as a function of total infrared luminosity ($L_{\text{IR}} = 1\text{-}1000 \mu\text{m}$). These are provided publicly, along with an IDL script for easily reading in the templates at http://www.cfa.harvard.edu/~dnarayan/DOG_SED_Templates.html

ACKNOWLEDGMENTS

We are grateful to Ranga-Ram Chary, Vandana Desai, Brandon Kelly, Kai Noeske, Jason Melbourne and Alex Pope for helpful conversations. D.N. thanks the NOAO in Tucson for hospitality, where part of this study was conducted. The authors are grateful to the W.M. Keck Foundation for hosting the Napa Galaxy Evolution workshop where the ideas for much of this project came

about. AD is supported by NOAO, which is operated by the Association of Universities for Research in Astronomy (AURA) under a cooperative agreement with the National Science Foundation. C.C.H. was funded by an NSF Graduate Research Fellowship. T.C. and M.B. acknowledge support from the W.M. Keck Foundation. RSB acknowledges financial assistance from HST grant GO10890, which is provided by NASA through a grant from the Space Telescope Science Institute which is operated by AURA under NASA contract NAS5-26555. PJ was supported by programs HST-AR-10678 and 10958, provided by NASA through a grant from the Space Telescope Science Institute, which is operated by the Association of Universities for Research in Astronomy, Incorporated, under NASA contract NAS5-26555, and by *Spitzer* Theory Grant 30183 from the Jet Propulsion Laboratory. Support for PFH was provided by the Miller Institute for Basic Research in Science, University of California, Berkeley. The simulations in this paper were run on the Odyssey cluster supported by the Harvard FAS Research Computing Group.

References

- Alexander D. M., Bauer F. E., Chapman S. C., Smail I., Blain A. W., Brandt W. N., Ivison R. J., 2005, *ApJ*, 632, 736
 Alexander D. M. et al., 2008, *AJ*, 135, 1968
 Armus L., Charmandaris V., Bernard-Salas J. et al., 2007, *ApJ*, 656, 148
 Barnes J. E., Hernquist L., 1996, *ApJ*, 471, 115
 Barnes J. E., Hernquist L. E., 1991, *ApJ*, 370, L65
 Baugh C. M. et al., 2005, *MNRAS*, 356, 1191
 Birnboim Y., Dekel A., Neistein E., 2007, *MNRAS*, 380, 339
 Blain A. W., Chapman S. C., Smail I., Ivison R., 2004, *ApJ*, 611, 725
 Blitz L., Rosolowsky E., 2006, *ApJ*, 650, 933
 Borys C., Smail I., Chapman S. C., Blain A. W., Alexander D. M., Ivison R. J., 2005, *ApJ*, 635, 853
 Bouché N. et al., 2007, *ApJ*, 671, 303
 Bournaud F., Daddi E., Elmegreen B. G. et al., 2008, *A&A*, 486, 741
 Bouwens R. J., Thompson R. I., Illingworth G. D. et al., 2004, *ApJ*, 616, L79
 Brand K., Dey A., Weedman D. et al., 2006, *ApJ*, 644, 143
 Brodwin M., Dey A., Brown M. J. I. et al., 2008, *ApJ*, 687, L65
 Bullock J. S., Kolatt T. S., Sigad Y., Somerville R. S., Kravtsov A. V., Klypin A. A., Primack J. R., Dekel A., 2001, *MNRAS*, 321, 559
 Bussmann R. S., Dey A., Borys C. et al., 2009, *ArXiv e-prints/0909.2650*
 Bussmann R. S., Dey A., Lotz J. et al., 2009, *ApJ*, 693, 750
 Calura F., Pipino A., Matteucci F., 2008, *A&A*, 479, 669
 Caputi K. I., Lagache G., Yan L. et al., 2007, *ApJ*, 660, 97
 Casey C. M., Chapman S. C., Beswick R. J. et al., 2009, *MNRAS*, pp 1231–
 Castor J., McCray R., Weaver R., 1975, *ApJ*, 200, L107
 Ceverino D., Dekel A., Bournaud F., 2010, *MNRAS*, pp 440–
 Chapman S. C., Casey C. M., 2009, *MNRAS*, 398, 1615
 Chapman S. C. et al., 2004, *ApJ*, 611, 732
 Chapman S. C., Windhorst R., Odewahn S., Yan H., Conselice C., 2003, *ApJ*, 599, 92
 Chary R., Elbaz D., 2001, *ApJ*, 556, 562
 Cox T. J., Jonsson P., Primack J. R., Somerville R. S., 2006, *MNRAS*, 373, 1013
 Croom S. M., Boyle B. J., Shanks T. et al., 2005, *MNRAS*, 356, 415
 Daddi E., Dannerbauer H., Elbaz D., Dickinson M., Morrison G., Stern D., Ravindranath S., 2008, *ApJ*, 673, L21
 Daddi E. et al., 2004, *ApJ*, 617, 746
 Daddi E. et al., 2005, *ApJ*, 631, L13
 Daddi E. et al., 2009, *ArXiv/0911.2776*
 Davé R., Finlator K., Oppenheimer B. D., Fardal M., Katz N., Kereš D., Weinberg D. H., 2009, *MNRAS Accepted: arXiv/0909.4078*
 Dekel A., Birnboim Y., Engel G. et al., 2008, *ArXiv e-prints*
 Dekel A., Birnboim Y., Engel G. et al., 2009, *Nature*, 457, 451
 Desai V., Soifer B. T., Dey A. et al., 2009, *ApJ*, 700, 1190
 Dey A. et al., 2009, in W. Wang, Z. Yang, Z. Luo, & Z. Chen ed., *Astronomical Society of the Pacific Conference Series Vol. 408 of Astronomical Society of the Pacific Conference Series, The Pedigrees of DOGs (Dust-Obscured Galaxies)*. pp 411–
 Dey A., Soifer B. T., Desai V. et al., 2008, *ApJ*, 677, 943
 Di Matteo T., Springel V., Hernquist L., 2005, *Nature*, 433, 604
 Dickinson M., Papovich C., Ferguson H. C., Budavári T., 2003, *ApJ*, 587, 25
 Donley J. L., Rieke G. H., Pérez-González P. G., Rigby J. R., Alonso-Herrero A., 2007, *ApJ*, 660, 167
 Dopita M. A., Groves B. A., Fischera J. et al., 2005, *ApJ*, 619, 755
 Downes D., Solomon P. M., 1998, *ApJ*, 507, 615
 Draine B. T., Li A., 2007, *ApJ*, 657, 810
 Dwek E. 1998, *ApJ*, 501, 643
 Elmegreen B. G. 2009, *ArXiv e-prints*
 Elmegreen B. G., Burkert A., 2010, *ApJ*, 712, 294
 Elmegreen D. M., Elmegreen B. G., Marcus M. T., Shahinyan K., Yau A., Petersen M., 2009, *ApJ*, 701, 306
 Elmegreen D. M., Elmegreen B. G., Ravindranath S., Coe D. A., 2007, *ApJ*, 658, 763
 Fakhouri O., Ma C.-P., 2008, *MNRAS*, 386, 577
 Farrah D., Lonsdale C. J., Weedman D. W. et al., 2008, *ApJ*, 677, 957
 Fiore F., Grazian A., Santini P. et al., 2008, *ApJ*, 672, 94
 Fiore F., Puccetti S., Brusa M. et al., 2009, *ApJ*, 693, 447
 Förster Schreiber N. M. et al., 2009, *ApJ*, 706, 1364
 Genzel R. et al., 2006, *Nature*, 442, 786
 Georgantopoulos I., Akylas A., Georgakakis A., Rowan-Robinson M., 2009, *ArXiv e-prints*
 Greve T. R. et al., 2005, *MNRAS*, 359, 1165
 Groves B., Dopita M. A., Sutherland R. S., Kewley L. J., Fischera J., Leitherer C., Brandl B., van Breugel W., 2008, *ApJS*, 176, 438
 Hernquist L. 1990, *ApJ*, 356, 359
 Hopkins A. M. 2004, *ApJ*, 615, 209
 Hopkins P. F., Bundy K., Croton D. et al., 2009, *ArXiv e-prints*
 Hopkins P. F. et al., 2005a, *ApJ*, 625, L71
 Hopkins P. F. et al., 2005b, *ApJ*, 630, 705
 Hopkins P. F. et al., 2006, *ApJS*, 163, 1
 Hopkins P. F. et al., 2008, *ApJS*, 175, 356
 Hopkins P. F., Hernquist L., 2010, *MNRAS*, 402, 985
 Hopkins P. F., Hernquist L., Cox T. J., Robertson B., Krause E., 2007, *ApJ*, 669, 45
 Hopkins P. F., Lidz A., Hernquist L., Coil A. L., Myers A. D., Cox T. J., Spergel D. N., 2007, *ApJ*, 662, 110
 Hopkins P. F., Richards G. T., Hernquist L., 2007, *ApJ*, 654, 731
 Hopkins P. F., Younger J. D., Hayward C. C., Narayanan D., Hernquist L., 2010, *MNRAS*, 402, 1693

- Houck J. R., Soifer B. T., Weedman D. et al., 2005, *ApJ*, 622, L105
- Huang J.-S., Faber S. M., Daddi E. et al., 2009, *ApJ*, 700, 183
- John T. L. 1988, *A&A*, 193, 189
- Jonsson P. 2006, *MNRAS*, 372, 2
- Jonsson P., Cox T. J., Primack J. R., Somerville R. S., 2006, *ApJ*, 637, 255
- Jonsson P., Groves B. A., Cox T. J., 2010, *MNRAS*, pp 186–
- Juvela M. 2005, *A&A*, 440, 531
- Kennicutt Jr. R. C. 1998, *ApJ*, 498, 541
- Kereš D., Katz N., Fardal M., Davé R., Weinberg D. H., 2009, *MNRAS*, 395, 160
- Kereš D., Katz N., Weinberg D. H., Davé R., 2005, *MNRAS*, 363, 2
- Kovács A. et al., 2006, *ApJ*, 650, 592
- Kovács A., Omont A., Beelen A. et al., 2010, *ArXiv e-prints*
- Lacy M., Storrie-Lombardi L. J., Sajina A. et al., 2004, *ApJS*, 154, 166
- Le Flocc'h E., Papovich C., Dole H. et al., 2005, *ApJ*, 632, 169
- Leitherer C. et al., 1999, *ApJS*, 123, 3
- Li A., Draine B. T., 2001, *ApJ*, 554, 778
- Li Y., Hernquist L., Robertson B. et al., 2007, *ApJ*, 665, 187
- Lidz A., Hopkins P. F., Cox T. J., Hernquist L., Robertson B., 2006, *ApJ*, 641, 41
- Lonsdale C. J., Polletta M. d. C., Omont A. et al., 2009, *ApJ*, 692, 422
- Lotz J. M., Jonsson P., Cox T. J., Primack J. R., 2008, *MNRAS*, 391, 1137
- Melbourne J., Bussman R. S., Brand K. et al., 2009, *AJ*, 137, 4854
- Melbourne J., Desai V., Armus L. et al., 2008, *AJ*, 136, 1110
- Menéndez-Delmestre K., Blain A. W., Alexander D. M. et al., 2007, *ApJ*, 655, L65
- Menéndez-Delmestre K., Blain A. W., Smail I. et al., 2009, *ApJ*, 699, 667
- Michałowski M. J., Hjorth J., Watson D., 2009, *ArXiv e-prints*
- Mihos J. C., Hernquist L., 1994, *ApJ*, 431, L9
- Mihos J. C., Hernquist L., 1996, *ApJ*, 464, 641
- Mo H. J., Mao S., White S. D. M., 1998, *MNRAS*, 295, 319
- Murphy E. J., Chary R.-R., Alexander D. M., Dickinson M., Mag-nelli B., Morrison G., Pope A., Teplitz H. I., 2009, *ApJ*, 698, 1380
- Narayanan D., Cox T. J., Hayward C. C., Younger J. D., Hernquist L., 2009, *MNRAS*, 400, 1919
- Narayanan D., Cox T. J., Kelly B. et al., 2008, *ApJS*, 176, 331
- Narayanan D., Hayward C. C., Cox T. J., Hernquist L., Jonsson P., Younger J. D., Groves B., 2009, *MNRAS* in press: arXiv/0904.0004
- Narayanan D., Hayward C. C., Cox T. J., Hernquist L., Jonsson P., Younger J. D., Groves B., 2010, *MNRAS*, 401, 1613
- Narayanan D., Kulesa C. A., Boss A., Walker C. K., 2006, *ApJ*, 647, 1426
- Narayanan D., Li Y., Cox T. J. et al., 2008, *ApJS*, 174, 13
- Pérez-González P. G., Rieke G. H., Egami E. et al., 2005, *ApJ*, 630, 82
- Pope A., Bussmann R. S., Dey A. et al., 2008, *ApJ*, 689, 127
- Pope A., Chary R.-R., Alexander D. M. et al., 2008, *ApJ*, 675, 1171
- Reddy N. A., Steidel C. C., Pettini M., Adelberger K. L., Shapley A. E., Erb D. K., Dickinson M., 2008, *ApJS*, 175, 48
- Richards G. T., Lacy M., Storrie-Lombardi L. J. et al., 2006, *ApJS*, 166, 470
- Rieke G. H., Alonso-Herrero A., Weiner B. J., Pérez-González P. G., Blaylock M., Donley J. L., Marcillac D., 2009, *ApJ*, 692, 556
- Rigby J. R., Rieke G. H., Maiolino R. et al., 2004, *ApJS*, 154, 160
- Robertson B., Hernquist L., Cox T. J., Di Matteo T., Hopkins P. F., Martini P., Springel V., 2006, *ApJ*, 641, 90
- Rosolowsky E. 2005, *PASP*, 117, 1403
- Rudnick G., Labbé I., Förster Schreiber N. M. et al., 2006, *ApJ*, 650, 624
- Sacchi N., La Franca F., Feruglio C. et al., 2009, *ArXiv e-prints*
- Sajina A., Yan L., Armus L., Choi P., Fadda D., Helou G., Spoon H., 2007, *ApJ*, 664, 713
- Sakamoto K. et al., 1999, *ApJ*, 514, 68
- Sanders D. B., Mirabel I. F., 1996, *ARA&A*, 34, 749
- Sanders D. B., Soifer B. T., Elias J. H., Madore B. F., Matthews K., Neugebauer G., Scoville N. Z., 1988, *ApJ*, 325, 74
- Shaver P. A., Wall J. V., Kellermann K. I., Jackson C. A., Hawkins M. R. S., 1996, *Nature*, 384, 439
- Shen Y., Strauss M. A., Oguri M. et al., 2007, *AJ*, 133, 2222
- Shi Y., Rieke G., Lotz J., Perez-Gonzalez P. G., 2009, *ApJ*, 697, 1764
- Simpson C., Eisenhardt P., 1999, *PASP*, 111, 691
- Soifer B. T., Helou G., Werner M., 2008, *ARA&A*, 46, 201
- Solomon P. M., Rivolo A. R., Barrett J., Yahil A., 1987, *ApJ*, 319, 730
- Springel V. 2005, *MNRAS*, 364, 1105
- Springel V., Di Matteo T., Hernquist L., 2005a, *ApJ*, 620, L79
- Springel V., Di Matteo T., Hernquist L., 2005b, *MNRAS*, 361, 776
- Springel V., Hernquist L., 2002, *MNRAS*, 333, 649
- Springel V., Hernquist L., 2003, *MNRAS*, 339, 289
- Swinbank A. M. et al., 2004, *ApJ*, 617, 64
- Swinbank A. M. et al., 2008, *MNRAS*, 391, 420
- Tacconi L. J. et al., 2006, *ApJ*, 640, 228
- Tacconi L. J. et al., 2008, *ApJ*, 680, 246
- Tacconi L. J. et al., 2010, *Nature*, 463, 781
- Tyler K. D., Flocc'h E. L., Rieke G. H. et al., 2009, *ApJ*, 691, 1846
- Valiante E., Lutz D., Sturm E., Genzel R., Tacconi L. J., Lehnert M. D., Baker A. J., 2007, *ApJ*, 660, 1060
- Vázquez G. A., Leitherer C., 2005, *ApJ*, 621, 695
- Vladilo G. 1998, *ApJ*, 493, 583
- Weedman D. et al., 2006a, *ApJ*, 653, 101
- Weedman D. W. et al., 2006b, *ApJ*, 651, 101
- Weingartner J. C., Draine B. T., 2001, *ApJ*, 548, 296
- Yan L., Chary R., Armus L. et al., 2005, *ApJ*, 628, 604
- Yan L., Sajina A., Fadda D. et al., 2007, *ApJ*, 658, 778
- Yan L., Tacconi L. J., Fiolet N. et al., 2010, *ApJ*, 714, 100
- Younger J. D. et al., 2008a, *ApJ*, 688, 59
- Younger J. D. et al., 2008b, *ApJ*, 686, 815
- Younger J. D., Hayward C. C., Narayanan D., Cox T. J., Hernquist L., Jonsson P., 2009, *MNRAS*, 396, L66
- Younger J. D., Omont A., Fiolet N. et al., 2009, *MNRAS*, 394, 1685